Engineering Structures 251 (2022) 113483

Contents lists available at ScienceDirect

Engineering Structures

journal homepage: www.elsevier.com/locate/engstruct

Response of shear critical reinforced concrete frames and walls under monotonic loading

H.M.S.S. Hippola [a], K.K. Wijesundara [a], Roberto Nascimbene [b]

[a] *Department of Civil Engineering, Faculty of Engineering, University of Peradeniya, Sri Lanka*
[b] *Scuola Universitaria Superiore IUSS Pavia, Piazza della Vittoria n.15, 27100 Pavia, Italy*

ARTICLE INFO

Keywords:
Force based finite element formulation
Moment-shear-axial interaction
Nonlinear static response
Shear critical reinforced concrete frames

ABSTRACT

This paper focuses on a novel finite element formulation which can predict the bending moment-shear force-axial force interaction of reinforced concrete frames and walls, and validate it against 170 experiments available in literature. This distributed plasticity element is established on force-based finite element method, where the relationship between element nodal forces and section forces are exactly known. Hence, element discretization is nonessential when modelling frames using this formulation, reducing the number of degrees of freedom in the numerical model compared to displacement-based formulations. The computations are carried out at four hierarchical levels, namely structure, element, section and fibre. There are two nested iterative procedures at the structure level and the section level. In the existing formulation, these iterative procedures are computationally demanding due to use of initial stiffness matrices. Furthermore, it uses Modified Compression Field Theory at the fibre level, which has inherent drawbacks compared to its more evolved version, the Disturbed stress Field Model. The current study refines the iterative procedures at structure and section levels to fully operate with tangent stiffness matrices to improve the speed of convergence. In addition, the Modified Compression Field Theory is replaced with the Disturbed stress Field Model at the fibre level to compute fibre resisting force for a given fibre deformation, accounting for both averaged behaviour and local crack slip. The novel element is validated by comparing the predicted results with experimental results of 170 tests found in the literature. It is shown that the novel element predicts the load carrying capacity well with an average experimental-to-predicted load carrying capacity ratio of 0.99 and a coefficient of variation of 12.8%. Furthermore, the element can be used to discuss the different failure mechanisms of reinforced concrete frame elements.

1. Introduction

Developing a robust, rational and computationally efficient numerical tool to perform nonlinear analyses of reinforced concrete (RC) frames accounting for bending moment-shear force-axial force (M-V-N) interaction is a challenging problem. Modelling RC frames with fibre beam-column elements have become popular over the years owing to its balanced accuracy of prediction and computational efficiency. The relationship between nodal forces and nodal deformations of such elements can be derived using displacement-based [1–4], force-based or mixed finite element methods [5–7]. Among these methods, force-based finite element method is preferred to be used with fibre beam-column elements as it waives the need for element discretization owing to the exactly known force interpolation functions [8–18]. The nonlinear force-based fibre beam-column element [19–21] included in OpenSees software [22] is widely used by the structural engineers to predict bending moment-axial force (M-N) interaction of RC frame structures. However, the structural engineers are still in short of a rigorous line element formulation to account M-V-N interaction. Guner and Vecchio [23,24] have introduced a displacement-based finite element formulation capable of predicting M-V-N interaction of RC frames incorporating Disturbed Stress Field Model (DSFM) [25] at the fibre level. In this formulation, element discretization is mandatory to get an approximately accurate curvature distribution along frame members, which increases the number of degrees of freedom (DOFs) required to model a structure. Furthermore, the global analysis of this formulation is performed using a single secant stiffness-based iterative procedure and it does not directly evaluate element or section level equilibrium. The implicit satisfaction of section equilibrium sometimes becomes inadequate to minimize section unbalanced forces and thus the iterative procedure fails to converge within the maximum number of iterative steps [26]. Addressing these issues, Rajapakse et al. (2019) [27], introduced a force-based fibre beam-column element formulation capable of predicting M-V-N interaction of RC frames and walls under static and monotonic loading conditions. This formulation uses Modified Compression Field Theory (MCFT) [28] as the constitutive relationship

https://doi.org/10.1016/j.engstruct.2021.113483
Received 2 March 2021; Received in revised form 26 September 2021; Accepted 23 October 2021
Available online 13 November 2021

at the fibre level. The element formulation is based on two nested iterative procedures at structure level and section level. The structure level iterative procedure minimizes the difference between external loads and structure resisting force while section level employs modified Newton-Raphson method to compute the updated section stiffness matrix for a given section force increment. Both of these iterative procedures operate with initial stiffness matrices, and as a result they consume a significant computational time. Furthermore, the MCFT implemented at fibre level, imposes a constraint that the principal stress directions and principal strain directions should coincide, does not calculate explicit slip deformations and consists of a cumbersome crack check.

This study aims to address the above issues and improve the formulation developed by Rajapakse et al. (2019) [27]. In the improved formulation, both iterative procedures fully operate with tangent stiffness matrices and are well harmonized to capture M-V-N interaction of RC frames and walls. The MCFT implemented at the fibre level is replaced with DSFM, allowing to explicitly calculate slip deformations of the fibres. The explicit computation of slip deformation releases the constraint that principal strain directions and principal stress directions should coincide. It further allows to omit computationally cumbersome crack check and provides a better representation of failure mechanisms. Furthermore, the shear strain profile of the sections is assumed to be parabolic throughout the analysis as it significantly reduces the computational time without compromising the accuracy of results in general engineering applications [29,30]. Furthermore, and in addition to the results used in the previous research [27], the improved element was experimentally validated against 170 reinforced concrete specimens available in literature. These specimens have varying shear span-depth ratios, percentages of longitudinal and transverse reinforcements, concrete strengths, section depths, boundary conditions and different failure modes. The proposed formulation is assessed for its accuracy of predicting load-deformation response, load-carrying capacity and failure mode.

2. Proposed formulation

The computations of the proposed formulation are based on four state determination procedures, namely structure state determination, element state determination, section state determination and fibre state determination, for an applied displacement increment.

The structure state determination computes the nodal force increment $\{\Delta \mathrm{F}\}$ and the nodal displacement increment $\{\Delta \mathrm{U}\}$ corresponding to a displacement increment $\Delta \mathrm{U}_2$ applied at the displacement controlling DOF. Fig. 1 provides an overview of the structure state determination. The element state determination computes the incremental element nodal resisting force vector, when the element nodal displacement increment vector of a particular structure level iteration is known. Fig. 2 presents an overview on the element state determination. The section state determination computes the updated section deformation and section stiffness matrix for a given section force increment, $\{\Delta \mathrm{S}\}_{\mathrm{i}}$. Fig. 3 presents an overview on the section state determination.

Once, $\{\Delta \mathrm{S}\}_{\mathrm{i}}$ of a particular section is known, the Newton-Raphson method is employed to iteratively find the updated section deformation and section stiffness matrix. A schematic diagram of section state determination is shown in Fig. 4. In the j$^{\mathrm{th}}$ section level iteration, the section deformation increment $\{\Delta e\}_j$, section stiffness matrix $[K^{\mathrm{sec}}]_j$, section resisting force $\{S_{res}\}_j$ and the section unbalanced force $\{\Delta S_{unb}\}_j$ are computed in sequence. The iterative procedure continues until the $\{\Delta S_{unb}\}_j$ vector becomes less than a specified tolerance value. More details of this process can be found in [31]- [33]

To calculate $\{S_{res}\}_j$ and $[K^{\mathrm{sec}}]_j$ for a given section deformation $\{e\}_j$, the axial stresses σ_x, shear stresses Γ_{xy}, and fibre stiffness matrices of all the fibres of the section should be computed. For this purpose, the DSFM can be used if the strain state at a point (axial strain ε_x, shear strain γ_{xy} and transverse strain ε_y) is known. For a given $\{e\}_j$, $\varepsilon_x$and γ_{xy} can be computed adhering to the assumptions that plane sections remain inplane and the shear strain variation through the depth of each section

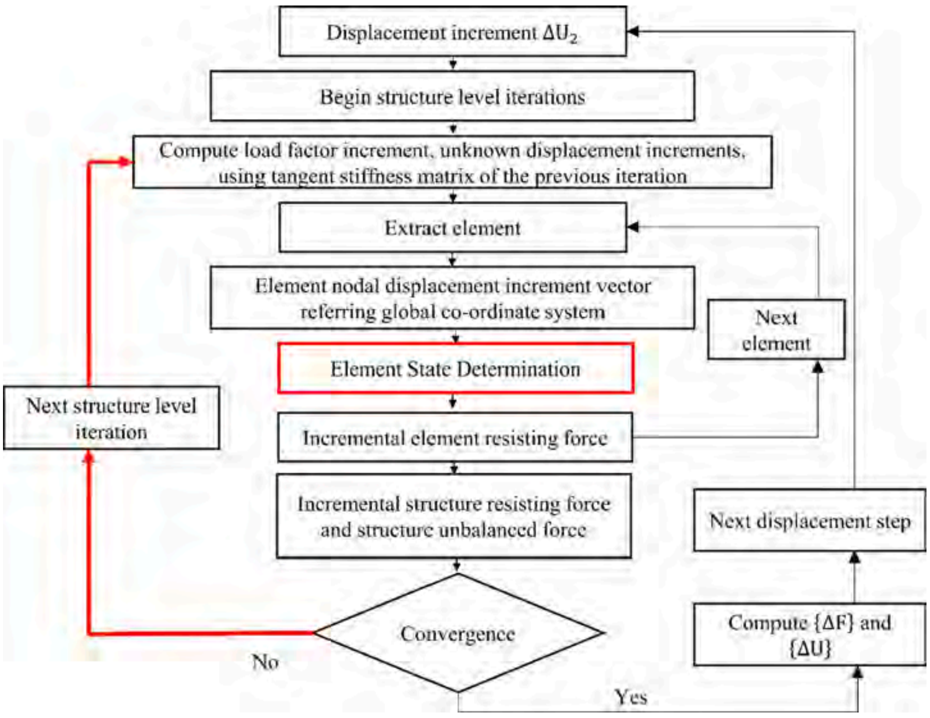

Fig. 1. Structure state determination.

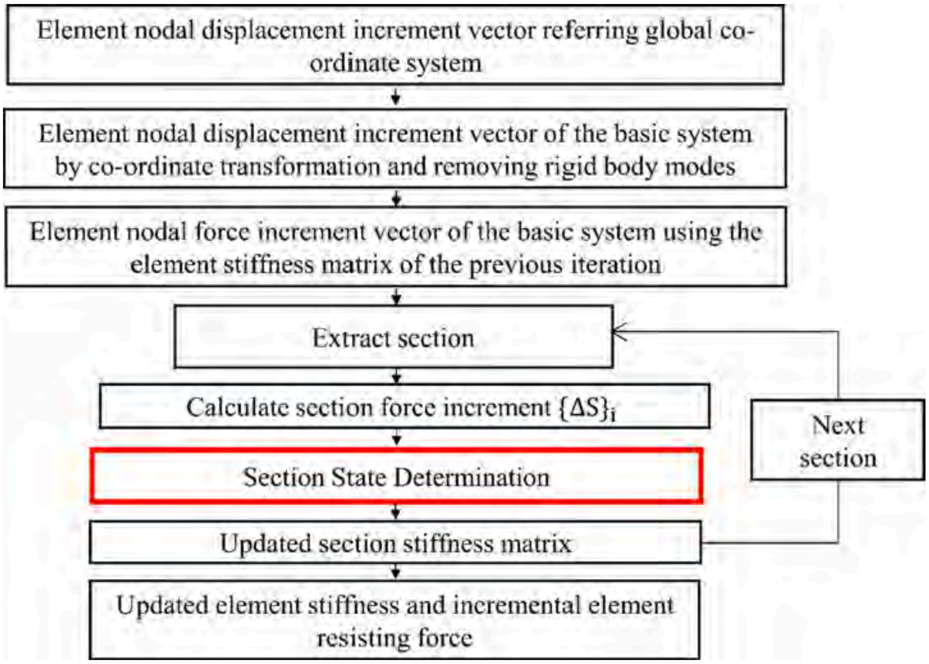

Fig. 2. Element state determination.

is parabolic. However, since the transverse strain component ε_y is an unknown, it is initially assumed as the transverse strain of the previous iteration. A solution algorithm is employed to compute the ε_y value which gives the transverse stress σ_y zero, which is a reasonable assumption when the section lies in a B-region. This process is summarized in Fig. 3. The constitutive model used to compute the stress state $\{\sigma_x\sigma_y\Gamma_{xy}\}$ when the strain state $\{\varepsilon_x\varepsilon_y\gamma_{xy}\}$ of a fibre is known, is discussed in the following section.

3. Constitutive model

The DSFM implemented at the fibre level is a smeared cracked concrete constitutive model which computes the averaged response of a fibre using uniaxial material models defined in principal directions. The averaged response is subsequently modified incorporating slip deformations computed at the local crack locations satisfying equilibrium.

Initially, the known net strain state $\left\{\varepsilon_x\varepsilon_y\gamma_{xy}\right\}^T$ and the previous slip deformation $\{\varepsilon^s_{previous}\}$ referring the x-y coordinate system of the fibre are used to derive the total strain state $\{\varepsilon_{tx}\varepsilon_{ty}\gamma_{txy}\}^T$, net principal strains (ε_{c1}, ε_{c2}) and principal stress orientation θ :

$$\{\varepsilon_{tx}\varepsilon_{ty}\gamma_{txy}\}^T = \{\varepsilon_x\varepsilon_y\gamma_{xy}\}^T + \{\varepsilon^s_{prev}\} \tag{1}$$

$$\varepsilon_{2,1} = \frac{\varepsilon_x + \varepsilon_y}{2} \mp \sqrt{\left(\frac{\varepsilon_x - \varepsilon_y}{2}\right)^2 + \left(\frac{\gamma_{xy}}{2}\right)^2} \tag{2}$$

$$\theta = \frac{1}{2}\tan^{-1}\left(\frac{\gamma_{xy}}{\varepsilon_y - \varepsilon_x}\right) \tag{3}$$

Subsequently, the net principal stresses (f_{c1}, f_{c2}) in concrete are computed using the uniaxial constitutive relationships defined in the principal directions. The post-cracking principal tensile stress f_{c1} is computed based on the dominant mechanism out of the tension stiffening [34] and tension softening (linear) mechanisms. The latter is dominant in lightly reinforced fibres located away from the main longitudinal bars while the former is dominant in well reinforced fibres. On the other hand, the principal compressive stress f_{c2} is calculated based on the Modified Kent and Park model [35] accounting compression softening [34] and confining effects [35]. At the same time, the transverse steel stress f_{sy} is computed based on the steel bilinear material model, assuming a perfect bond between steel and concrete. Subsequently, the fibre tangent and secant stiffness matrices are derived:

$$[D_{tangent}] = T_{rot}^T \begin{bmatrix} \frac{df_{c1}}{d\varepsilon_1} & 0 & 0 \\ 0 & \frac{df_{c2}}{d\varepsilon_2} & 0 \\ 0 & 0 & \frac{0.5(f_{c1} - f_{c2})}{\varepsilon_{c1} - \varepsilon_{c2}} \end{bmatrix} T_{rot} + \begin{bmatrix} 0 & 0 & 0 \\ 0 & p_y\frac{df_{sy}}{d\varepsilon_y} & 0 \\ 0 & 0 & 0 \end{bmatrix} \tag{4}$$

$$[D_{secant}] = T_{rot}^T \begin{bmatrix} \frac{f_{c1}}{\varepsilon_{c1}} & 0 & 0 \\ 0 & \frac{f_{c2}}{\varepsilon_{c2}} & 0 \\ 0 & 0 & \frac{\frac{f_{c1}}{\varepsilon_{c1}}\frac{f_{c2}}{\varepsilon_{c2}}}{\frac{f_{c1}}{\varepsilon_{c1}} + \frac{f_{c2}}{\varepsilon_{c2}}} \end{bmatrix} T_{rot} + \begin{bmatrix} 0 & 0 & 0 \\ 0 & p_y\frac{f_{sy}}{\varepsilon_y} & 0 \\ 0 & 0 & 0 \end{bmatrix} \tag{5}$$

where p_x, p_y and T_{rot} are respectively the smeared reinforcement ratios of the fibre in x, y directions and the transformation matrix:

$$T_{rot} = \begin{bmatrix} \cos^2\theta & \sin^2\theta & \cos\theta\sin\theta \\ \sin^2\theta & \cos^2\theta & -\cos\theta\sin\theta \\ -2\cos\theta\sin\theta & 2\cos\theta\sin\theta & \cos^2\theta - \sin^2\theta \end{bmatrix} \tag{6}$$

In the next stage, the local crack shear stress V_{ci} of the fibre is computed based on the equilibrium, compatibility and steel constitutive relationship at local cracks. Based on V_{ci}, the slip displacement of the fibre is computed using both the stress-based approach [36] and the constant lag-based approach as described in [25]. To find the slip deformation vector$\{\varepsilon^s\}$, the maximum slip displacement along cracks obtained out of the two approaches is transformed in to the fibre local co-ordinate system (x,y). Detailed descriptions of these computations can be found in [23,26], and [37]. Subsequently, the stress state of a fibre can be computed using Eq. (7):

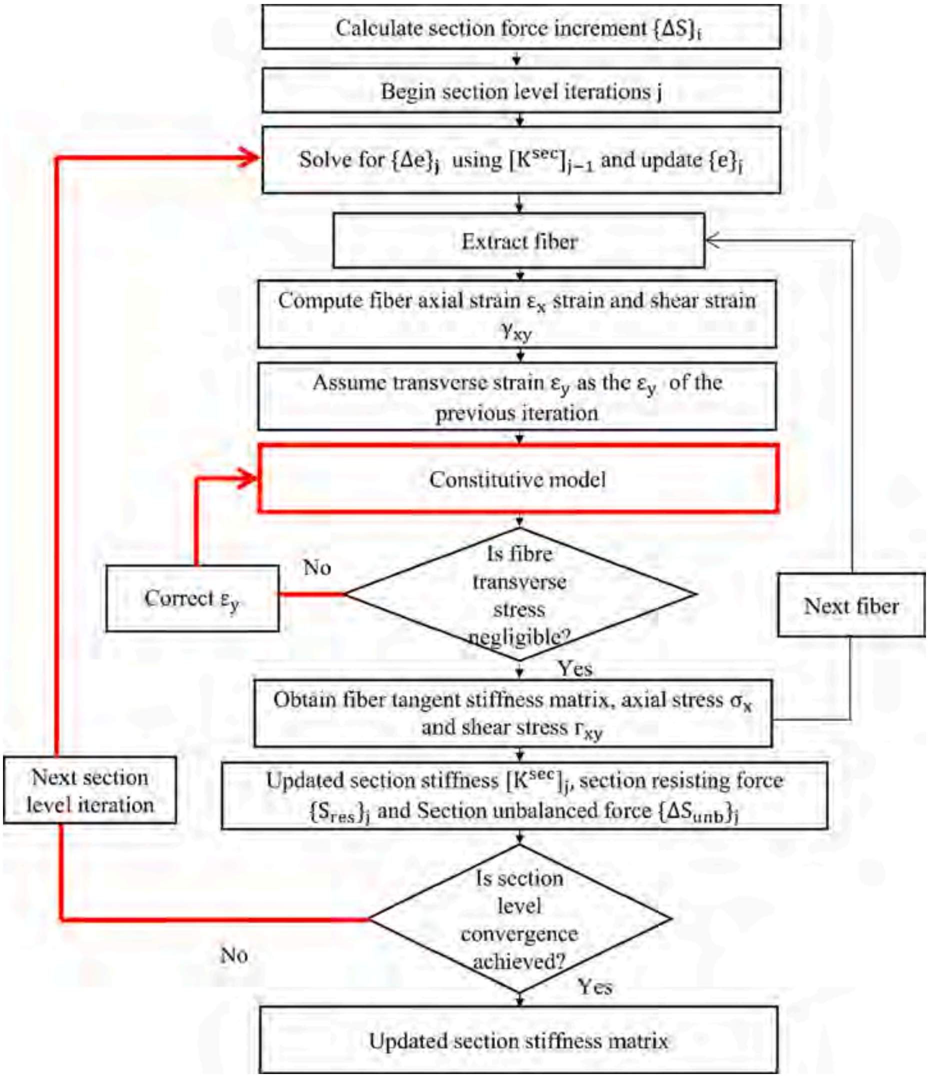

Fig. 3. Section state determination.

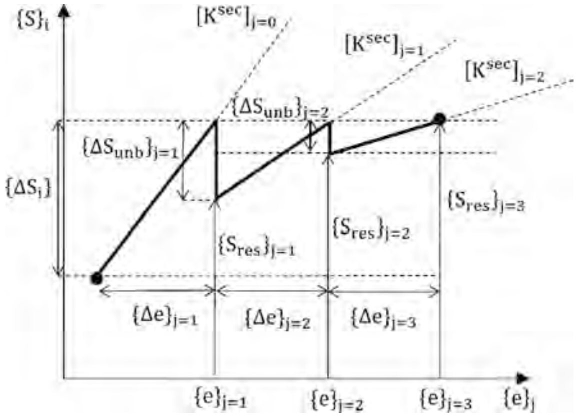

Fig. 4. Schematic diagram of section level iterative procedure.

$$\begin{Bmatrix}\sigma_x\\ \sigma_y\\ \Gamma_{xy}\end{Bmatrix} = [D_{secant}]\{\varepsilon_{tx}\varepsilon_{ty}\gamma_{txy}\}^T - [D_{c,secant}]\{\varepsilon^s_{previous}\} \tag{7}$$

The explicit computation of slip deformation $\{\varepsilon^s\}$ releases the constraint that principal strain directions and principal stress directions should coincide. It further allows to omit computationally cumbersome crack check and provides a better representation of failure mechanisms.

4. Experimental database

The proposed formulation is validated against 170 reinforced concrete specimens found in literature including 161 simply supported beams, 6 shear walls, and 3 planar frames. The specimens are selected from experimental studies of Bresler and Scoredelis (1963) [38], Krefeld and Thurston (1966) [39], Lefas et al. (1990) [40], Vecchio and Balopoulou (1990) [41], Vecchio and Emara (1992) [42], Angekolas et al. (2001) [43], Vecchio and Shim (2004) [44], Duong et al. (2007) [45], and Sherwood et al. (2007) [46]. In the selected specimens, shear span-depth ratio varies from 2 to 9.8, percentage of longitudinal reinforcement ratio varies from 0.5% to 3.96%, percentage of transverse reinforcement ratio varies from 0% to 0.8%, depth varies from 0.3 m to 1.51 m, and concrete strength varies from 12.2 MPa to 48.5 MPa. The geometry, loading conditions, material properties, experimental load carrying capacities (V_{exp}), and predicted load carrying capacities (V_{pred}) of all the specimens are given in Appendix I.

5. Results and discussion

This section presents a detailed discussion on the load-deformation responses and the failure modes of selected simply supported beams, shear walls and planar frames.

5.1. Simply supported beams

All the simply supported beams are modelled using two elements, each of which have 6 integration points. Each integration point is assigned a fibre section that is discretized in to 60 number of layers. The norm for force tolerance at the structure and section level iterative procedures is 0.001. The schematic diagram given in Fig. 5 shows the element and section numbering of the numerical model.

The first set of beams selected for the validation is the classic beam test series in Bresler and Scordelis (1963) [38], which is extensively used as benchmark data for calibrating and verifying models for RC beams, especially when they are shear critical. The testing has been carried out on 12 simply supported beams loaded monotonically at the mid span. The details of the specimens are given in Appendix I.

The experimental load-deformation responses are compared with the predicted responses as illustrated in Fig. 6. The comparison shows excellent agreement in terms of the initial stiffness, post-cracking stiffness and load carrying capacity of beams B2, C2, OA2, A3, B3, C3, and OA3. However, an over-estimation of the post-cracking stiffness could be observed in beams A1, A2, B1, C1 and OA1 which have the lowest shear span to depth ratios. The imposed section kinematic assumption of parabolic shear strain variation along the depth of the section may leads to an under-estimation of the shear strains in the tensile zone of the beam [1]. As a result, the beam displacement may be under-estimated in the post-cracking branch, in beams with significant shear deformations.

The experimental failure modes of the above twelve beams were reported to be of three different modes, namely shear-compression failures, diagonal-tension failures, and flexure-compression failures. The following discussion presents how these experimental failure modes are predicted in the analytical results obtained from the proposed formulation.

5.1.1. Shear-compression failure

In this experimental program, the beam specimens A1, A2, B1, B2, C1 and C2 were reinforced in both longitudinal and transverse directions and they had shear span-depth ratios of 4 and 5 for series 1 and series 2 beams, respectively. These specimens displayed diagonal shear cracks distributed in the shear span region. The failures of these beams were observed as concrete crushing in the compression zone near the loading plate due to the combined effects of flexure and shear. The following discussion presents how the failure mode of beam specimen A1 is predicted in the numerical model.

The principal compressive stress, principal tensile stress and shear stress variations along the depths of all the integration points of element 1 (see Fig. 5 for integration point/ section numbering), at the failure of the beam specimen A1 are shown in Fig. 7(a)-(c), respectively. The principal compressive stress variation of sections 5 and 6 in Fig. 7(a) illustrates that the top fibres have reached the peak compressive strength. Furthermore, the predicted crack orientations in Fig. 8(e) illustrate the inclination of the concrete compression direction near the loading point. These observations confirm the initiation of concrete crushing in an inclined direction near the loading point due to combined action of shear and bending. This predicted failure mode is consistent with failure mode observed in the experiment.

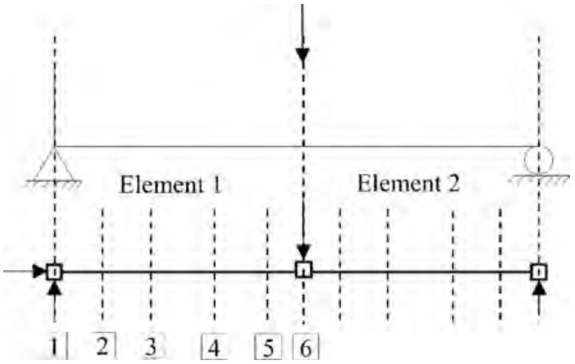

Fig. 5. Element numbering and section/ integration point numbering of the numerical model for simply supported beams.

In the proposed algorithm, the pre-cracking tensile response of a fibre in the first principal direction is linear-elastic while the post-cracking response is governed by either tension softening or tension stiffening models, based on which phenomenon is dominant. If the fibre is well reinforced, the tension stiffening mechanism becomes dominant, while the tension softening mechanism becomes dominant when the fibre is lightly reinforced or unreinforced. Due to the three different tension carrying mechanisms, the principal tensile stress given in Fig. 7 (b) display a discontinuous variation. The top fibres behave linear-elastically in tension while tension softening model govern the tensile behaviour of middle fibres due to their low reinforcement ratios. At failure, the principal tensile stress of these middle fibres has reached zero in sections 2 to 5, as the tension softening model reaches zero tensile stress at relatively lower strain compared to tension stiffening model. The zero principal tensile stresses observed in the middle fibres in the sections 2 to 5 reflect the generation of diagonal shear cracks distributed along the shear span as shown in the crack width diagram given in Fig. 7(e). Furthermore, significant slip deformations were also predicted at these cracks as evident from crack slip diagram in Fig. 7(d).

5.1.2. Diagonal-tension failure

It was reported in the experiment that, the beam specimens without transverse reinforcement OA1, OA2, and OA3, fail suddenly with the opening of a single major diagonal-tension crack. The proposed formulation is capable of numerically predicting this failure mode as discussed in the following referring beam specimen OA2.

When using the proposed formulation to model RC members without transverse reinforcement, some of the fibres which are away from longitudinal steel bars will be locally unreinforced in both directions. In such fibres, the post-cracking principal tensile stress will be governed only by the tension softening phenomenon. Once the principal tensile strain of such fibres in a particular section reaches the terminal strain of the tension softening mechanism, the principal tensile stress of those fibres will become zero. As a result, the crack widths of those fibres will be significantly increased with the application of displacement increments. When a crack width as high as 20 mm is numerically predicted, the formulation will predict the failure of that element. Fig. 8 shows the variation of principal compressive stress, principal tensile stress and shear stress along the depths of all the integration points of element 1, just before the failure of the beam OA2. The principal tensile stress variations in Fig. 8(b) illustrate that the tension softening effect has become zero in the locally unreinforced middle fibres in section 4. Subsequently, a large crack width is numerically predicted on those fibres, simulating the single dominant diagonal crack observed in the experiment.

The beam A1 discussed in section 5.1.1 has transverse reinforcement and develops a number of significant inclined shear cracks distributed in the shear span. In contrast, the beam specimen OA2 discussed here is unreinforced in the transverse direction and it fails by forming a single dominant shear crack. These failure modes are consistent with the predicted principal tensile stress variations at failure, shown in Figs. 7(b) and 8(b). In the beam specimen A1, the principal tensile stress of mid fibres of all the sections in the shear span have reached zero (Fig. 7(b)) reflecting the distribution of cracks in the shear span. In the beam specimen OA2, the principal tensile stress has reached zero only in a single section (see Fig. 8(b)) reflecting the generation of a single dominant diagonal crack. Furthermore, the shear-compression crushing previously observed in beam A1 is not observed in beam OA2.

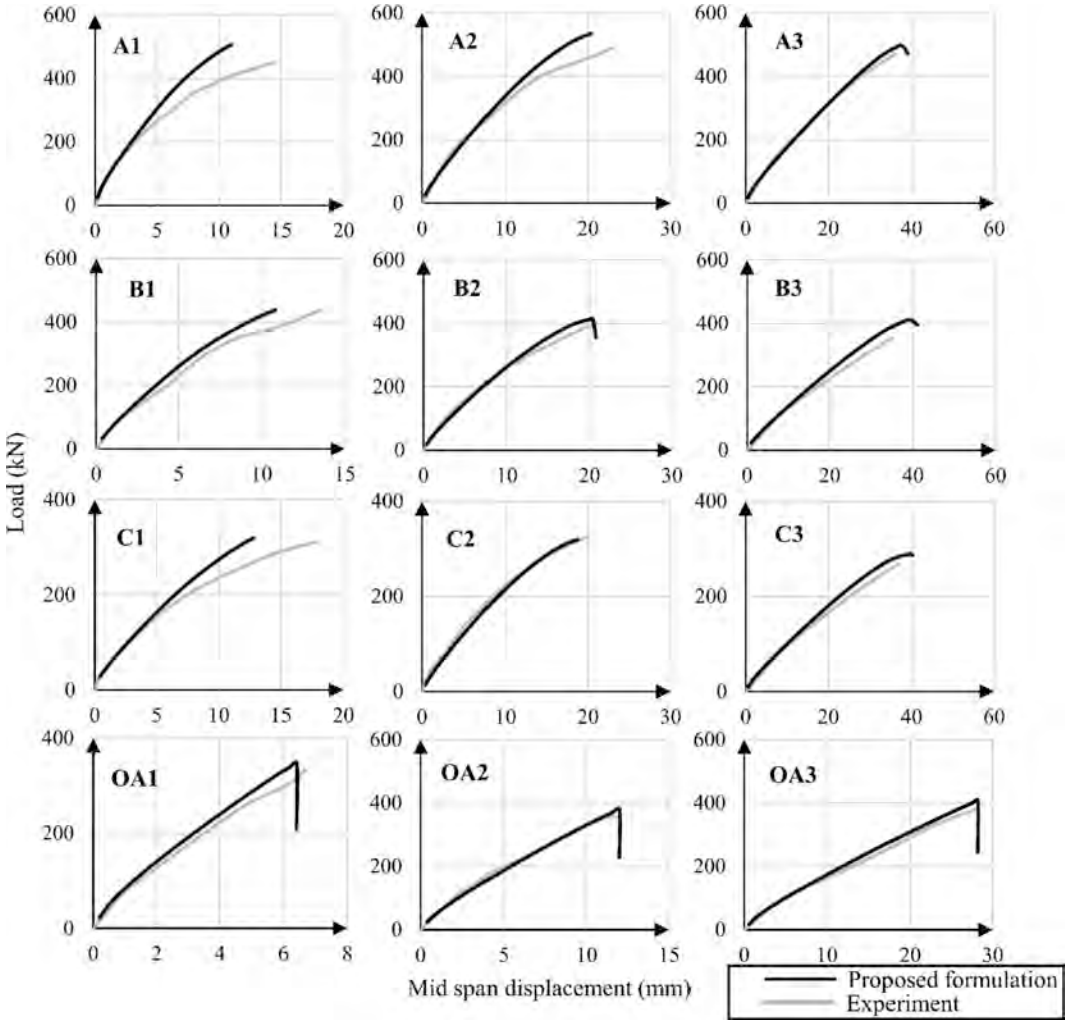

Fig. 6. Load deformation comparison of Bresler and Scordelis (1963) beams.

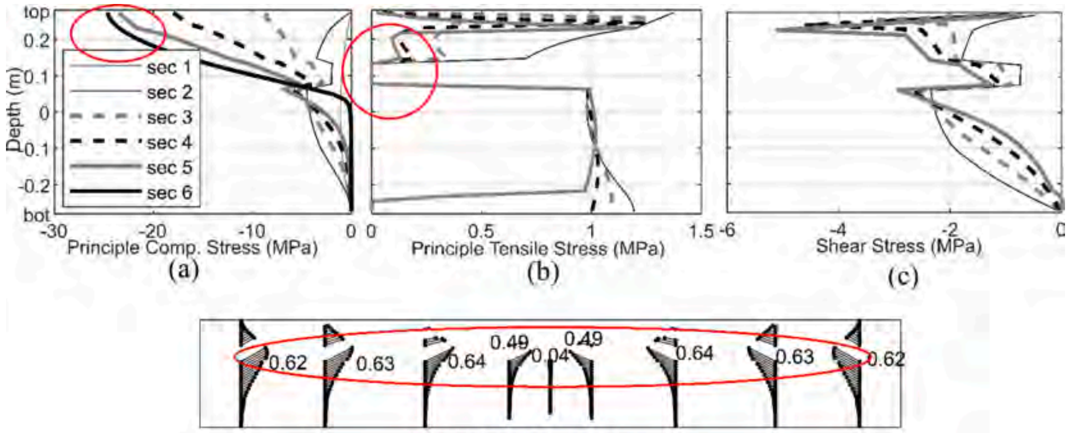

(a) (b) (c)

(d) Crack slips in mm

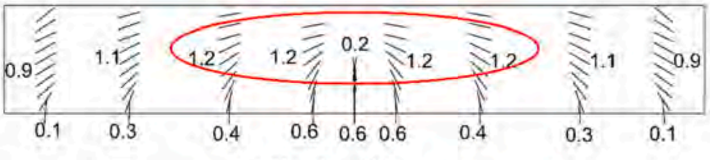

(e) Crack widths in mm

Fig. 7. Sectional plots of A1 at failure.

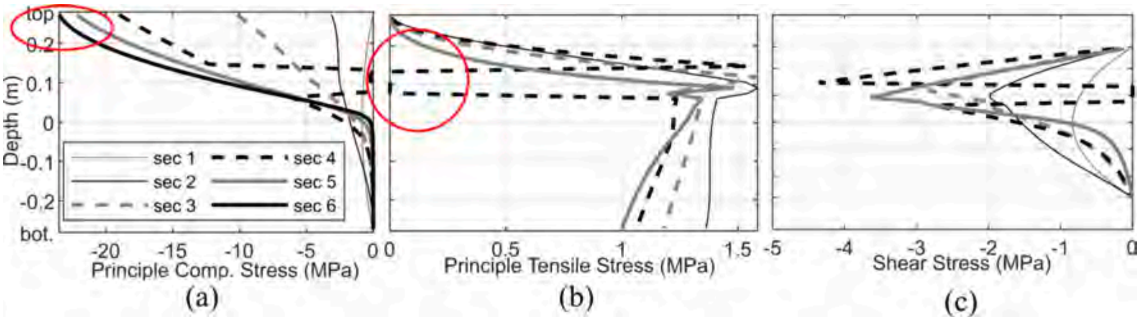

Fig. 8. Sectional plots of OA2 at failure.

5.1.3. *Flexure-compression failures*

The beam specimens A3, B3, and C3 were reinforced in both directions and have relatively higher shear span to depth ratio of 7. It was reported in the experiment that they develop significant flexural cracks at the bottom and fail by flexure-driven compression crushing of concrete near the loading point. The proposed formulation is capable of numerically predicting this failure mode as discussed in the following referring beam specimen A3.

Fig. 9(a)-(c) show the principal compressive stress, principal tensile stress and shear stress variations of the beam specimen A3 along the depths of all the integration points of element 1. The principal compressive stress variation of section 6 in Fig. 9(a) illustrates the degradation of principal compressive stresses in the top fibres near the loading point. The predicted crack pattern shown in Fig. 9 (e) illustrates that the principal compressive directions of fibres in the compression zone are approximately horizontal. These observations confirm that the crushing of concrete occurs in an approximately horizontal direction near the loading point mainly due to flexural effects. This predicted failure mode is consistent with failure mode observed in the experiment.

The beam A1 discussed in section 5.1.1 has a relatively low shear span-depth ratio and thus has a higher shear deformation compared to the relatively slender beam A3 discussed here. Due to higher shear deformations, the compression direction of A1 near the loading point is inclined while it is approximately horizontal in beam A3. Therefore, the concrete crushing in A1 occurs in an inclined direction due to both shear and flexural effects while the compression crushing of A3 occurs in an approximately horizontal direction governed by only flexural effects. Furthermore, the principal tensile stresses in the mid fibres of A3 have not reached zero implying that the shear cracks are not dominant in the shear span. This argument can be further strengthened by observing the crack slip and crack width diagrams in Fig. 9(d) and 9(e).

Another experimental program was carried out at the University of Toronto to investigate the shear capacity of large lightly reinforced concrete beams [43]. This program aimed to examine the effect of longitudinal reinforcement and concrete compressive strength on the shear capacity of large lightly reinforced members with and without transverse reinforcement. Twelve simply supported beams having a depth of 1 m, width of 0.3 m and a shear span to depth ratio of 2.7 were monotonically loaded at the mid span until failure. The details of these beams are summarized in Appendix I. The comparisons of the experimental and numerical load-deformation responses are given in Fig. 10.

The initial stiffnesses of the beams are accurately predicted, however a deviation of the stiffness is observed in all the specimens after the initiation of flexural cracks at the bottom of the beams. This deviation can be explained by the assumption of parabolic shear strain variation along the section depths which can underestimate the shear strains in the tensile zone and thus the beam shear deformation when the members are deep. Furthermore, the behaviour of large concrete beams with low unevenly distributed reinforcement is governed by the concrete cracking strength and the post-cracking tension softening phenomenon.

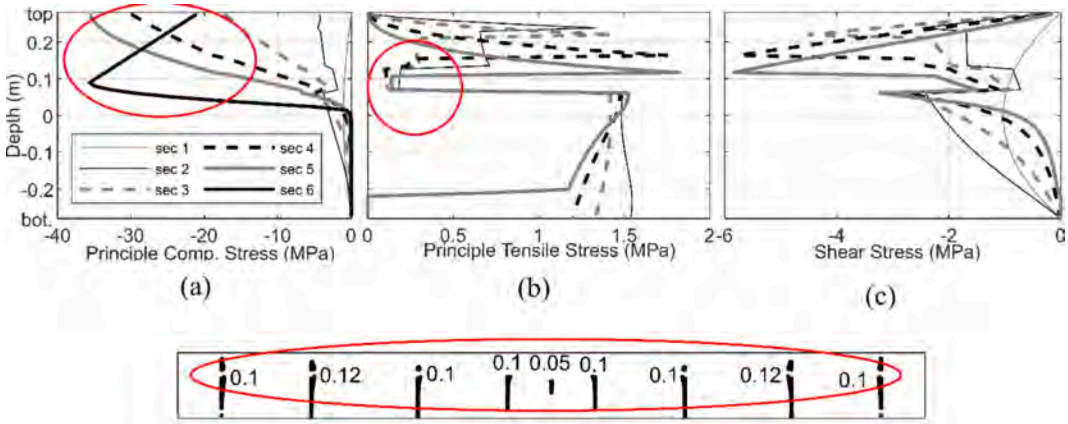

(d) Crack slips in mm

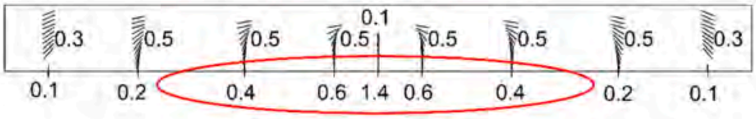

(e) Crack widths in mm

Fig. 9. Sectional plots of A3 at failure.

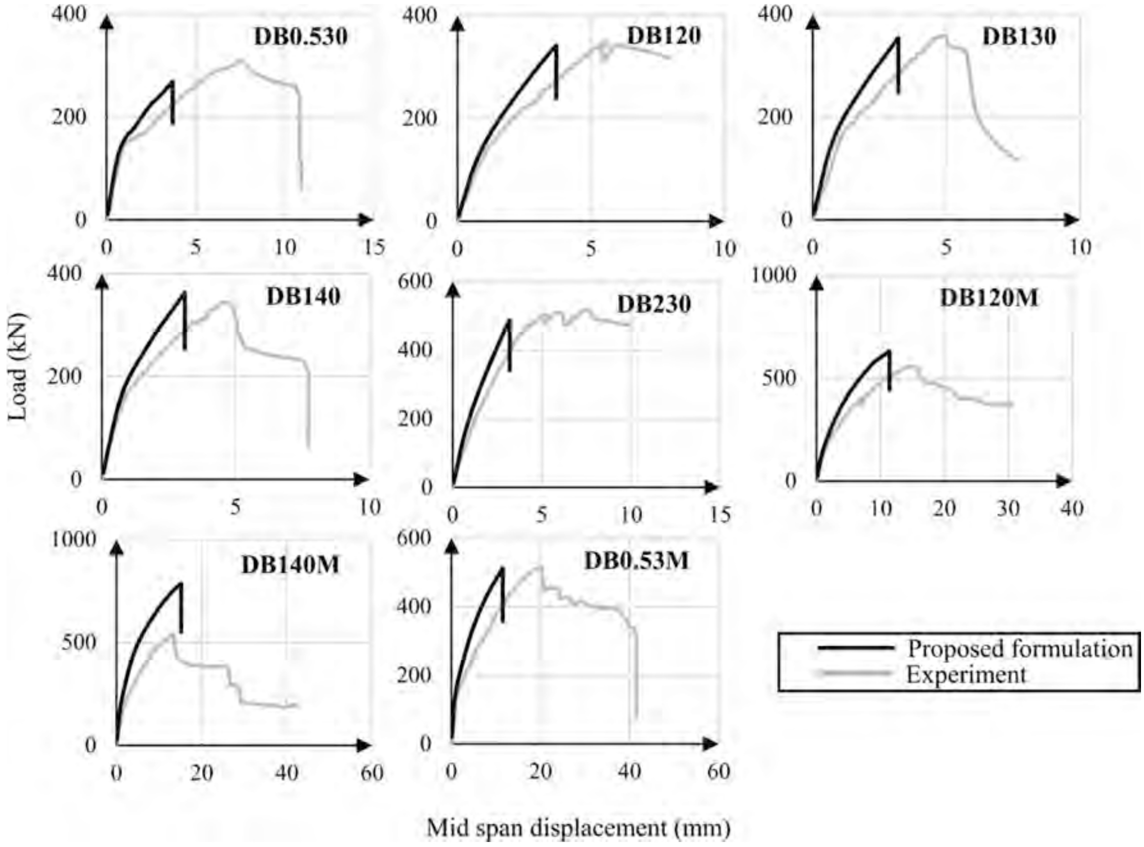

Fig. 10. Load deformation comparison of Angekolas et al. (2001) beams.

The scattered nature of concrete cracking strength prediction and the use of linear tension softening model might have not accurately modelled the actual post-cracking tensile behaviour in the experiment, which can cause a stiffness over-prediction. Even though there is a deviation in post-cracking stiffness, the load-carrying capacities of the beams are predicted with good accuracy. The failure modes of all the specimens were accurately predicted by the proposed formulation as diagonal-tension failures. Single major diagonal cracks were numerically predicted in all the beams as discussed in the failure mode of beam specimen OA2 in the section 5.1.2. The experimental post-peak behaviour of all the beams except DB230 display a sudden drop of strength at the load carrying capacity and then retain a degrading residual strength. This sudden strength drop is due to the generation of a major diagonal crack in the shear span of the beams. The proposed formulation is capable of predicting the load carrying capacity of the beams, however it cannot predict the residual strengths after the

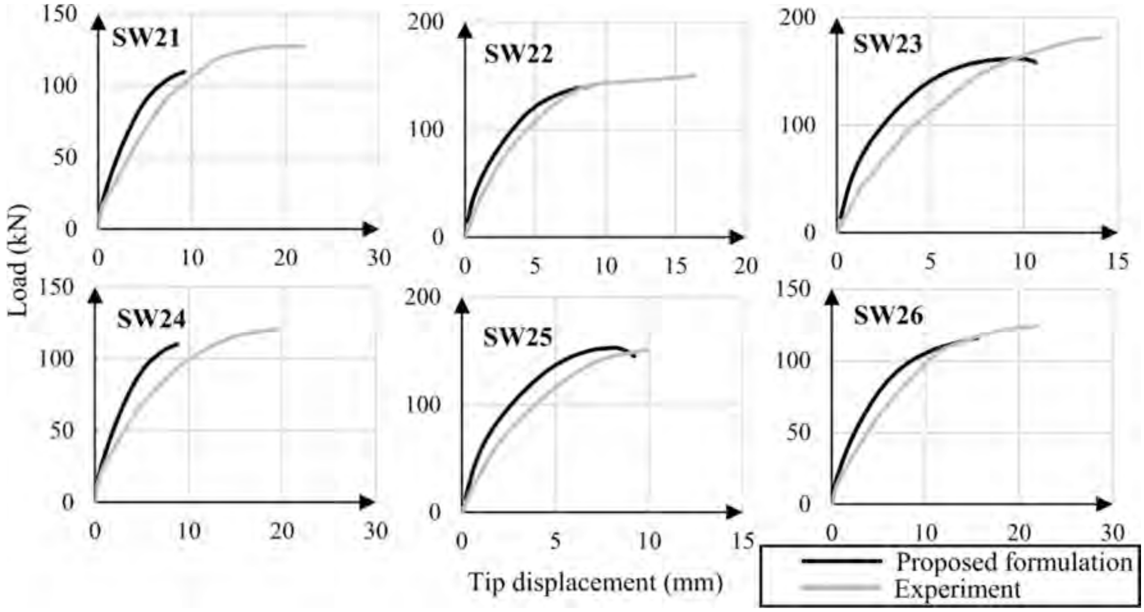

Fig. 11. Load deformation comparison of Lefas et al. (1990) shear walls.

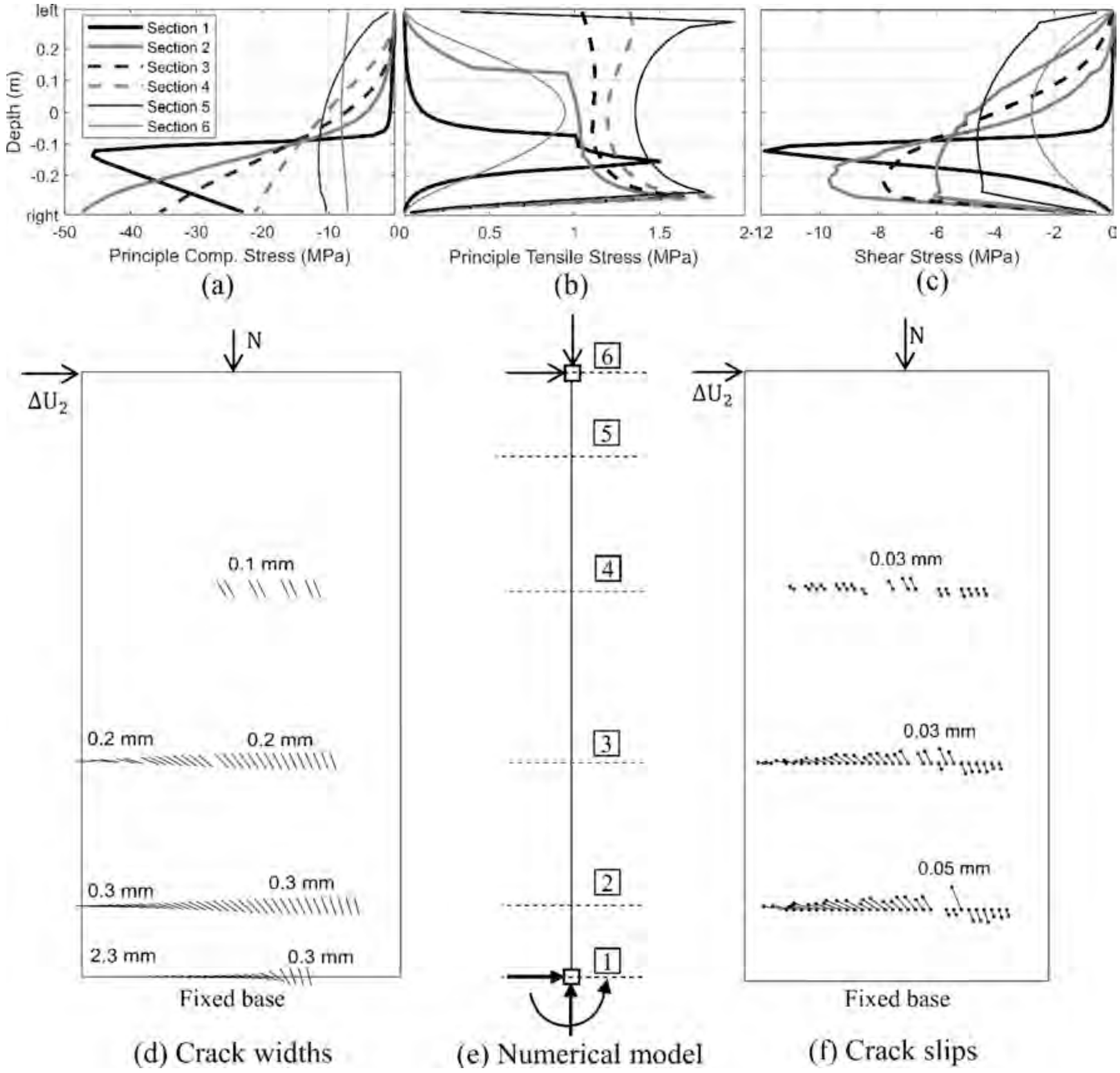

Fig. 12. Sectional plots of SW23 at failure.

generation of a single dominant diagonal crack. The residual strength and related displacement predictions of these kinds of beams are very difficult through sectional analyses algorithms and require further study. Furthermore, modelling high strength beams too require further study and thus high strength beams in this series were not modelled using the proposed formulation.

5.2. *Shear walls*

Six cantilever shear walls were selected from the experimental program conducted by Lefas et al. (1990) [40] at the Imperial College, London. The walls were subjected to constant axial loads and a monotonically increasing horizontal loads on the tip. The details of these walls are summarized in Appendix I.

Each wall is modelled using a single element having six Gauss-Lobatto integration points. The fibre sections at each integration point are discretized into 40 number of layers. Both structure level and section level iterative procedures are assigned with a force norm tolerance of 0.001. The comparison of experimental and numerical load-deformation responses given in Fig. 11 are in good agreement in terms of initial stiffness and load carrying capacity. A deviation of post-cracking stiffness was observed again as in previous analyses, which can be explained by the under-prediction of the shear deformation in the tensile zone when assuming parabolic shear strain variations along the depth of the sections.

The predicted failure modes of these shear walls are governed by crushing of concrete in the compression zone at the base of the walls, due to the combined action of axial force, bending moment and shear force. A series of significant inclined cracks and slip displacements are predicted along the wall height as shown in Fig. 12 (d) and (f), while the wall failure occurred due to inclined crushing of concrete near the wall base as shown in Fig. 12 (a). These results are consistent with the experimentally observed failure mode.

5.3. *Planar frames*

The first RC frame used for the validation is a two-storey single bay frame, experimented by Duong et al. (2007) [45]. Fig. 13 shows the loading arrangement, geometry and cross-sectional details of the frame. The motivation for this experimental study was to observe the behaviour of the first storey beam, which was intentionally designed to fail in shear. The testing of the frame was carried out in two phases, namely A and B, where in phase A, the frame was loaded until significant shear damage occur and the loading was subsequently reversed. In phase B, the frame was repaired and tested again for a sequence of complete cycles at multiples of yield displacement. The numerical predictions from the proposed formulation are compared with the results from phase A.

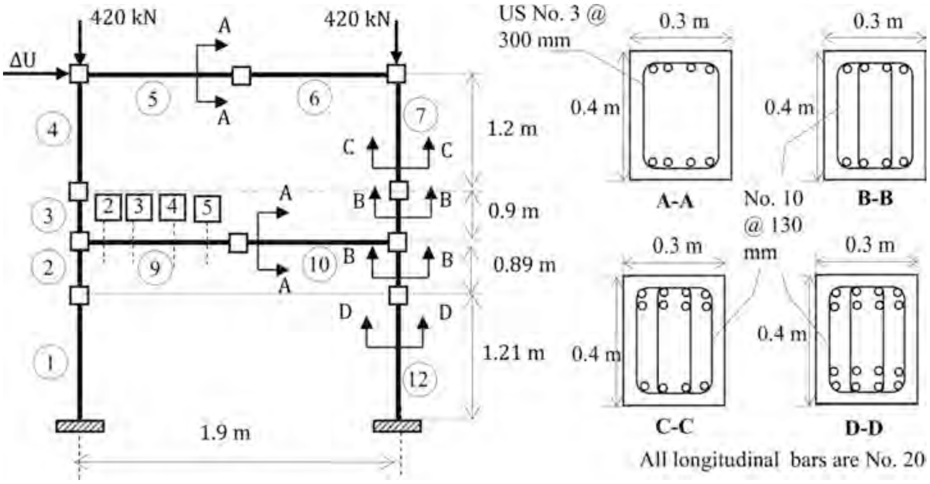

Fig. 13. Loading arrangement, geometry and cross-sectional details of Duong et al. (2007) frame [45].

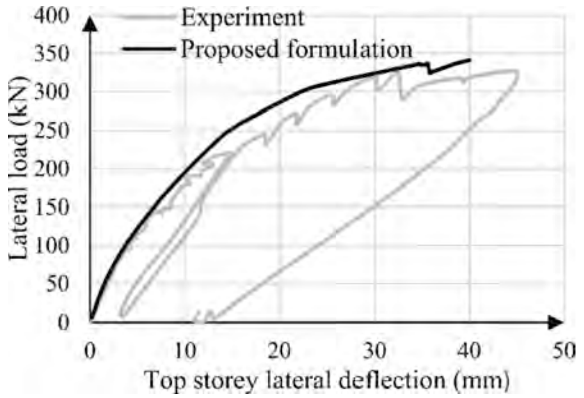

Fig. 14. Experimental and analytical load-deformation response Duong frame [45].

The frame is modelled using 12 elements as shown in Fig. 13. Each element is monitored at 6 Gauss-Lobatto integration points and each section is discretized in to 30 number of layers. The analysis is carried out by applying 0.2 mm lateral displacement steps. Both the structure level and section level iterative procedures converged to a force norm of 0.001. It is evident from Fig. 14 that the analytical and experimental load-deformation responses are in good agreement. However, a slight over-estimation of post-cracking stiffness is observed along with a slight under-estimation of the ultimate displacement which are in line with the observations made in previously analysed RC beams and walls.

The experimental loads and analytical loads for significant events of the frame behaviour are summarized and compared in Table 1. The load levels for initiation of flexure and shear cracks, yielding of longitudinal and transverse reinforcement and the peak load are predicted with a good accuracy.

Table 1
Comparison of experimental and numerical predictions of Duong frame [45].

Observed frame behaviour	Experimental load (kN)	Analytical load (kN)	Percentage difference (%)
Flexural cracks at first- and second-storey beams	75	58	29.3
Shear cracks at the first-storey beam	148	136	8.8
Yielding of longitudinal steel at beam ends of the first-storey	295	253	16.6
Yielding of stirrups of the first storey beam	320	321	−0.3
Peak load	326	335	−2.7

The experimental failure mode of the frame was governed by a single dominant diagonal-tension crack in the first storey beam, due to its low transverse reinforcement ratio. In the numerical results, the failure is observed in the second section of element 9 (see Fig. 13), where the principal tensile stresses of the mid fibres reached zeros due to yielding of transverse reinforcement. This behaviour is not observed in other sections of element 9 which reflects that there is only one dominant diagonal-tension crack. These observations are consistent with the experimentally observed failure mode and also follows the diagonal-tension failure mode discussed for beams with low transverse reinforcement ratios in Section 6.1.2.

The second frame used for the validation of the proposed element is a large scale, two-storey single bay planar RC frame tested by Vecchio and Emara (1992) [42] with the aim of observing the shear deformations of RC frames. Fig. 15 shows the geometry, loading arrangement and cross-sectional details. More details of the material properties can be found in [42].

The frame is modelled using 8 of the proposed elements, where each element is monitored at 6 Gauss-Lobatto integration points. Each integration point is discretized in to 60 number of layers. The analysis is carried out by applying 0.6 mm displacement steps with a force norm tolerance of 0.001 at both section level and structure level iterative procedures. The experimental and analytical load-deformation responses are shown in Fig. 16.

The initial stiffness of the frame is accurately predicted, however, a slight over prediction of stiffness is observed after the initial concrete cracking. The load carrying capacity and the frame stiffness after longitudinal reinforcement yielding are accurately predicted. The plateau of post-peak ductility is predicted accurately for a certain extent; however, the full ductility is not captured by this model as it neglects the effects of geometrical nonlinearity.

The experimental failure mode was observed due to development of plastic hinges at the first storey beam ends and column bases. The predicted sectional plots at failure, show the reinforcement yielding and the concrete crushing at the first storey beam ends and column bases. The crack patterns illustrated that the concrete crushing at these locations occur in an approximately parallel direction to the beam/ column orientation which implies flexure dominant cracking. These observations are consistent with the experimental failure mode and they follow the failure mode of flexure critical beam A3 discussed in section 6.1.3.

The third frame used for the validation of the proposed element is a two-storey single bay RC frame, monotonically loaded vertically from the first storey beam mid span experimented by Vecchio and Balopoulou

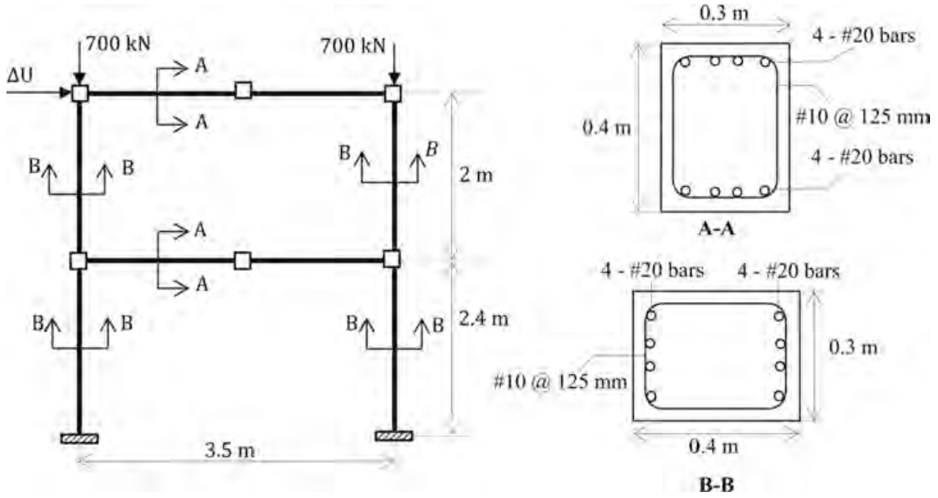

Fig. 15. Geometry, loading arrangement, and cross-sectional details of Vecchio and Emara (1992) frame [42].

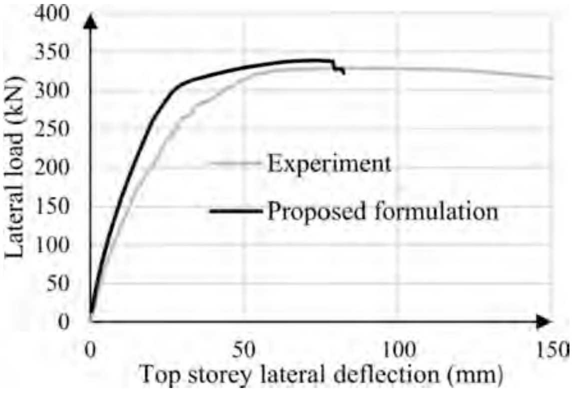

Fig. 16. Experimental and analytical load-deformation responses of Vecchio and Emara (1992) frame.

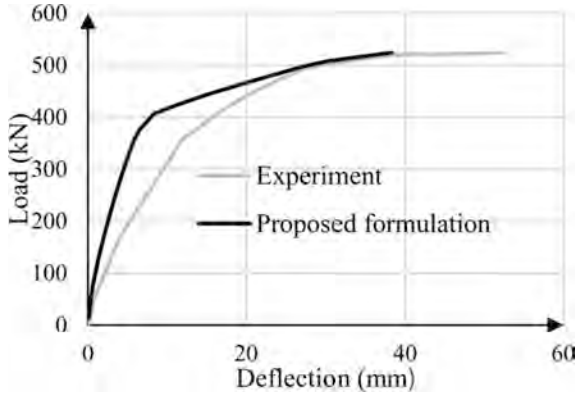

Fig. 18. Experimental and analytical load-deformation responses of Vecchio and Balopoulou (1990) frame [41].

(1990) [41]. The details about the geometry, loading arrangement, and the cross-sectional details are shown in Fig. 17.

The frame is modelled using 9 elements, where each element is monitored at 4 Gauss-Lobatto integration points. Each integration point is discretized in to 40 layers. The analysis was carried out by applying 0.1 mm displacement steps and the force norm tolerance is taken as 0.001 for both structure and section level iterative procedures. The comparison of analytical and experimental load-deformation responses is shown in Fig. 18.

The load-carrying capacity of the frame is predicted with very good accuracy. However, the stiffness of the frame, prior to yielding of reinforcement is different in the experimental and numerical responses. This difference can be explained by the significant drying related shrinkage

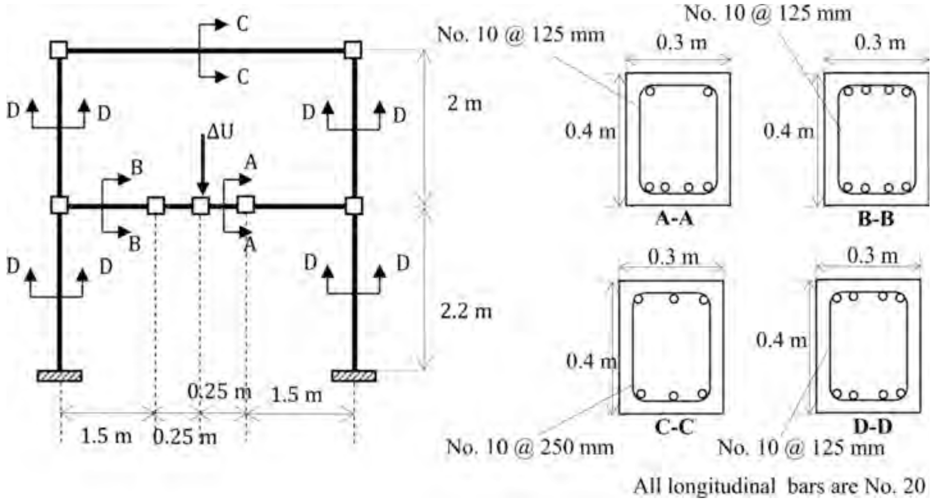

Fig. 17. Geometry, loading arrangement, and cross-sectional details of Vecchio and Balopoulou (1990) frame [41].

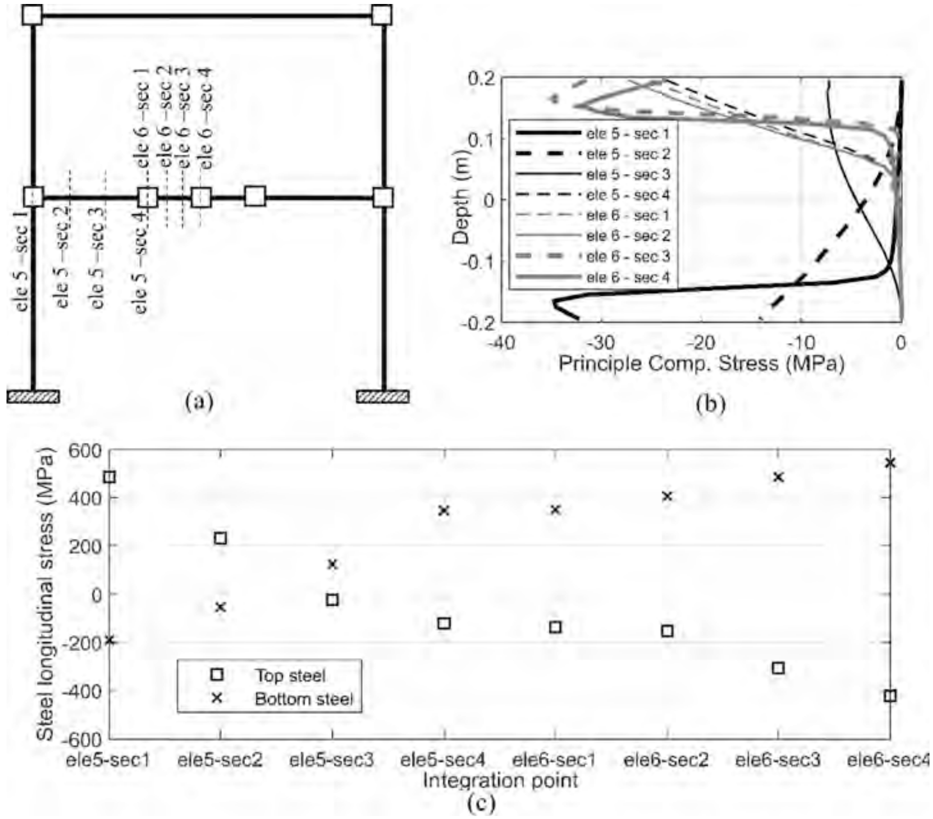

Fig. 19. Sectional plots of ele 5 and 6 of Vecchio and Balopoulou (1990) frame at failure.

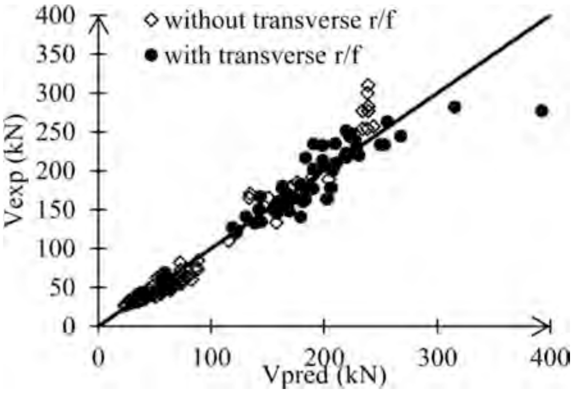

Fig. 20. Experimental and predicted load carrying capacities of all the specimens.

cracks (0.2–0.25 mm) observed in the experiment, as they lead to an experimental load-deformation response with significantly lower stiffness. The experimental failure mode of the frame was reported as formation of plastic hinges at first storey beam ends and the mid span. The numerically predicted principal compressive stress diagram in Fig. 19(b) demonstrate the compression crushing at the first storey beam ends and mid span. The stresses of top and bottom steel shown in Fig. 19(c) demonstrate the yielding of longitudinal steel (fy = 418 MPa) at the beam ends and the mid span.

These observations imply the development of plastic hinges at first storey beam ends and mid span.

6. Summary of the experimental validation

In this section, a summary of load-carrying capacity predictions of 167 RC specimens is presented. The details of the 161 beams, and 6 walls are summarized in Appendix I. Fig. 20 shows the predicted and experimental load carrying capacities with respect to the 45° line.

The proposed formulation produces an average load carrying capacity experimental-to-predicted ratio of 0.99 with a coefficient of variation (COV) of 12.8%. The most conservative prediction is 1.3 while the most un-conservative prediction is 0.7.

Fig. 21(a)-(e) illustrate the distribution of experimental-to-predicted load carrying capacity ratios $\frac{V_{exp}}{V_{pred}}$ of all the specimens with respect to shear span to depth ratios (a/d), longitudinal reinforcement ratios (p_x), transverse reinforcement ratios (p_y) , beam depths (d) and concrete compressive strengths $f_c^{'}$, respectively. These graphs illustrate that the RC specimens selected for the experimental validation cover wide ranges of a/d, p_x, p_y, d, and $f_c^{'}$ values. Fig. 21(f) illustrates the distribution of experimental-to-predicted ultimate displacements $\frac{\delta_{ult,exp}}{\delta_{ult,pred}}$ for the RC specimens discussed in this paper.

The proposed element formulation under-estimates the ultimate displacement of members with low shear span to depth ratios. Two sources could be identified for this inaccuracy; the imposed kinematic constraint of parabolic shear strain variation along the depth of the section under-estimates the contribution of shear deformation to the displacement, and the inability of sectional analysis algorithms to predict post-peak behaviour of shear critical members which have shear-compression or diagonal-tension failure modes. However, the capacity predictions from the proposed formulation show a consistent distribution in all the ranges of these parameters showing the applicability of the proposed formulation for a wide range of reinforced concrete frames and walls to predict shear capacity.

7. Conclusions

This paper presents a novel force-based line element formulation

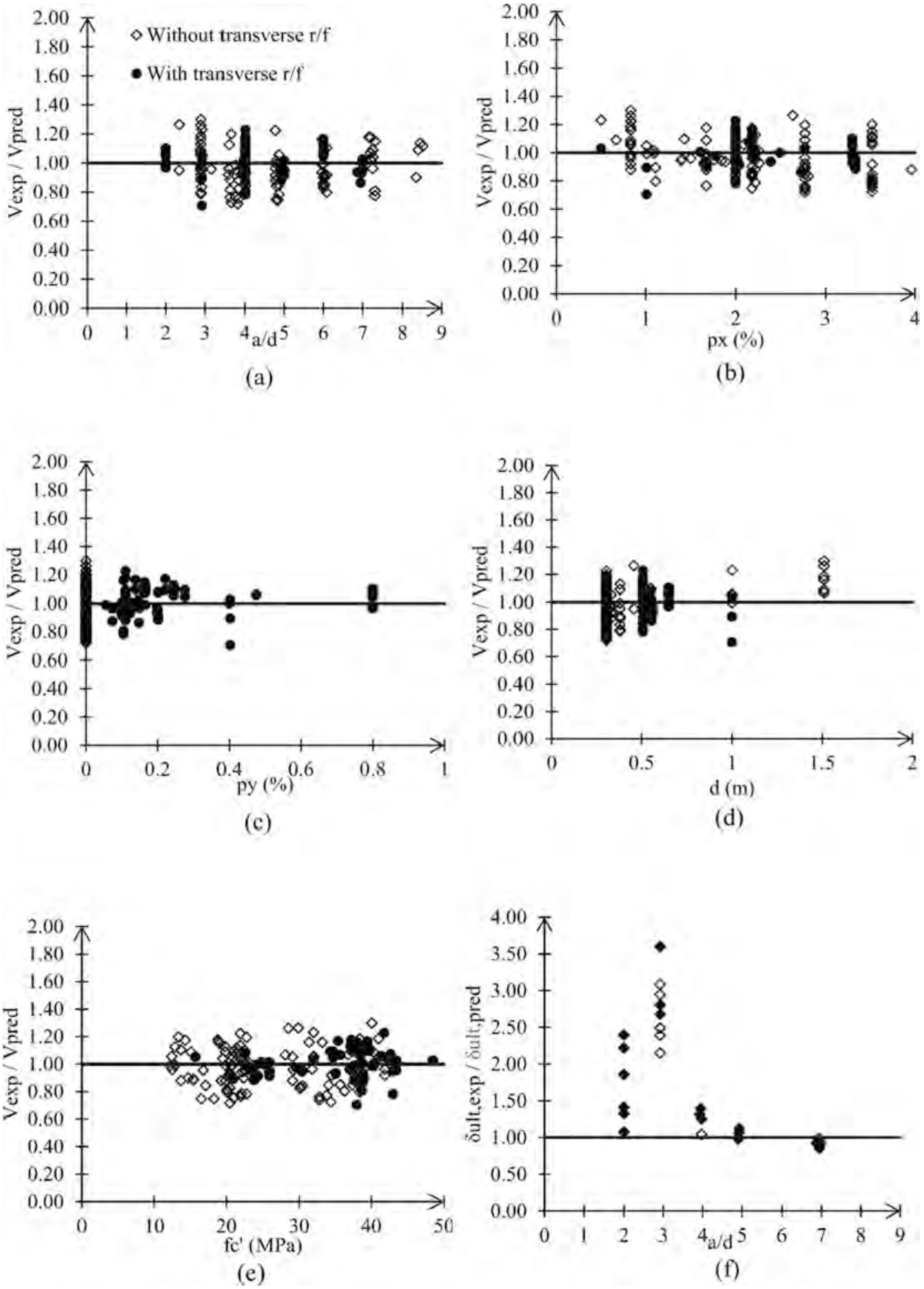

Fig. 21. Experimental and predicted load carrying capacities with respect to different parameters.

which accounts for bending moment-shear force-axial force interaction of reinforced concrete and its application to predict the response reinforced concrete beams, walls and frames found in literature. Unlike in displacement-based line element formulations, element discretization is not required since the force interpolation functions are exactly known through equilibrium. The formulation is based on the distributed plasticity method and kinematic constraints of plane section remain plane and parabolic shear strain variation along the depth of the section are imposed at the section level. There are two nested iterative procedures at structure level and section level. Both iterative procedures work with tangent stiffness matrices and thus the convergence is faster than in element formulations which utilize initial and secant stiffness matrices for the iterative procedures. At the fibre level, the Disturbed Stress Field Model (DSFM) is implemented as the constitutive relationship. The DSFM relieves the constraint that the principal stress and strain direction of a material point should coincide and facilitates the explicit computation of the slip deformations. The proposed line element formulation was validated against an experimental database with 170 specimens. The selected specimens had varying shear span-depth ratios from 2 to 9.8, longitudinal reinforcement ratios from 0.5% to 3.96%, transverse reinforcement ratios from 0% to 0.8%, depths from 0.3 m to 1.51 m, and concrete strengths from 12.2 MPa to 48.5 MPa. The load-deformation responses were in good agreement in terms of initial stiffness, initial tensile cracking, and load carrying capacity. The load carrying capacity of the 170 specimens were accurately predicted, with a mean experiment-to-predicted ratio of 0.99 and a COV of 12.8%. In addition, the proposed element also displayed the capability to accurately predict shear-compression, diagonal-tension and flexure-compression failure modes. However, the prediction of the ultimate displacements of shear critical members was unsatisfactory and two sources of inaccuracies were identified, which require further study. First, in the post-cracking branch, the sectional kinematic constraint of parabolic shear strain variation leads to an under-estimation the shear strains in the tensile zone and subsequently the element displacements, resulting a stiffer load-deformation response. Secondly, the proposed formulation is unable to predict the strength degradation and corresponding displacements for the shear-compression and the diagonal-tension failure modes. These draw-backs limits the usage of the current formulation in the calculation of ductility demands and energy dissipations of shear critical elements. However, the proposed element formulation is suitable to identify shear critical members in large frame structures with many elements, predict distribution of internal forces, crack patterns of members, load carrying capacities, and failure modes, which are important in the ultimate limit state design of frame structures, assessment of the safety of existing structures prone to brittle failures and determination of suitable retrofitting strategies.

CRediT authorship contribution statement

H.M.S.S. Hippola: Conceptualization, Methodology, Software, Writing – original draft. **K.K. Wijesundara:** Conceptualization, Methodology, Investigation, Resources. **Roberto Nascimbene:** Writing – review & editing, Supervision.

Declaration of Competing Interest

The authors declare that they have no known competing financial interests or personal relationships that could have appeared to influence the work reported in this paper.

Appendix A

F6No.	ID	b (m)	h (m)	L_s(m)	$\frac{a}{d}$	$f_c^{'}$(MPa)	a_g(mm)	ρ_x(%)	f_{yx}(MPa)	ρ_y(%)	f_{yy} (MPa)	V_{exp} (kN)	V_{pred}(kN)	$\frac{V_{exp}}{V_{pred}}$
Bresler and Scordelis (1963) – Simply supported beams														
1	BS-OA1	0.31	0.556	1.83	3.97	22.6	19	1.5	555	0	–	167	173.8	0.96
2	BS-OA2	0.305	0.561	2.29	4.9	23.7	19	1.88	555	0	–	178	190	0.94
3	BS-OA3	0.307	0.556	3.2	6.93	37.6	19	2.27	552	0	–	189	204	0.93
4	BS-A1	0.307	0.561	1.83	3.92	24.1	19	1.64	[345 555 555]	0.1	325	233.5	253.1	0.92
5	BS-A2	0.305	0.559	2.29	4.93	24.3	19	2.04	[345 555 555 555]	0.101	325	244.5	267.4	0.91
6	BS-A3	0.307	0.561	3.2	6.87	35.1	19	2.39	[345 552 552]	0.1	325	233.5	249.3	0.94
7	BS-B1	0.231	0.556	1.83	3.97	24.8	19	2.2	[345 555 555]	0.147	325	222.5	218.9	1.02
8	BS-B2	0.229	0.561	2.29	4.91	23.2	19	2.2	[345 555 555]	0.148	325	200	206.8	0.97
9	BS-B3	0.229	0.556	3.2	6.95	38.8	19	2.73	[345 552 552 552]	0.148	325	178	206.1	0.86
10	BS-C1	0.155	0.559	1.83	3.95	29.6	19	1.78	[345 555 555]	0.199	325	155.5	159.5	0.97
11	BS-C2	0.152	0.559	2.29	4.92	23.8	19	3.33	[345 555 555]	0.202	325	162.5	183.6	0.89
12	BS-C3	0.155	0.554	3.2	6.98	35.1	19	3.3	[345 552 552]	0.199	325	134.5	144.4	0.93
Krefeld and Thurston (1966) – Simply supported beams														
13	II4A3	0.203	0.457	0.91	2.34	30.6	25	1.76	400	0	–	109.9	115.6	0.95
14	II5A3	0.203	0.457	0.91	2.34	29.9	25	2.64	400	0	–	170.4	134.8	1.26
15	II11A2	0.152	0.381	0.91	2.91	30.2	25	2.82	400	0	–	73.4	88.02	0.83
16	II12A2	0.152	0.305	0.91	3.85	30.1	25	3.52	400	0	–	64.05	77.72	0.82
17	III18A2	0.152	0.381	0.91	2.89	19.3	25	2.22	370	0	–	63.16	71.69	0.88
18	III18B2	0.152	0.381	0.91	2.89	19.9	25	2.22	370	0	–	72.06	72.64	0.99
19	III18C2	0.152	0.381	0.91	2.89	22.6	25	2.22	370	0	–	73.4	77.18	0.95
20	III18D2	0.152	0.381	0.91	2.89	22.1	25	2.22	370	0	–	60.05	76.29	0.79
21	IV13A2	0.152	0.381	0.91	2.87	19.9	25	0.67	379	0	–	48.49	44.46	1.09
22	IV14A2	0.152	0.305	0.91	3.77	20.7	25	0.84	379	0	–	35.14	35.66	0.99
23	IV15A2	0.152	0.381	0.91	2.89	20.1	25	1.11	370	0	–	45.82	57.48	0.8
24	IV15B2	0.152	0.381	0.91	2.89	20.7	25	1.11	370	0	–	52.04	58.14	0.9
25	IV16A2	0.152	0.305	0.91	3.81	22.2	25	1.39	370	0	–	41.81	44.24	0.95
26	IV17A2	0.152	0.305	0.91	3.77	22	25	1.67	379	0	–	44.04	57.45	0.77
27	IV18E 2	0.152	0.381	0.91	2.89	19.8	25	2.22	370	0	–	81.85	72.51	1.13
28	IV19A2	0.152	0.305	0.91	3.81	20.5	25	2.78	370	0	–	46.26	64.29	0.72
29	IV20A2	0.152	0.305	0.91	3.85	21	25	3.52	400	0	–	50.71	67.07	0.76
30	IV21A2	0.203	0.305	0.91	3.85	19.9	25	3.96	400	0	–	76.51	86.88	0.88
31	V1AC	0.152	0.305	1.22	4.77	21.9	25	0.84	379	0	–	32.92	26.88	1.22
32	V2AC	0.152	0.305	1.22	4.8	23	25	1.09	394	0	–	37.81	37.26	1.01
33	V3AC	0.152	0.305	1.22	4.77	20.8	25	1.67	379	0	–	44.04	48.21	0.91
34	V4AC	0.152	0.305	1.22	4.8	16.5	25	2.18	394	0	–	37.81	50.52	0.75
35	V5AC	0.152	0.305	1.22	4.83	18.3	25	2.78	370	0	–	41.81	55.8	0.75
36	V6AC	0.152	0.305	1.22	4.87	22.8	25	3.52	400	0	–	53.38	68.09	0.78
37	V1CC	0.152	0.305	1.52	5.96	18.9	25	0.84	379	0	–	26.69	22.95	1.16
38	V2CC	0.152	0.305	1.52	6	20.8	25	1.09	394	0	–	30.25	30.44	0.99
39	V3CC	0.152	0.305	1.52	5.96	20.5	25	1.67	379	0	–	35.59	38.06	0.93
40	V4CC	0.152	0.305	1.52	6	20.5	25	2.18	394	0	–	40.03	48.45	0.83
41	V5CC	0.152	0.305	1.52	6.04	20.3	25	2.78	370	0	–	44.48	48.15	0.92

(*continued on next page*)

(*continued*)

F6No.	ID	b (m)	h (m)	L_s(m)	$\frac{a}{d}$	$f_c^{'}$(MPa)	a_g(mm)	ρ_x(%)	f_{yx}(MPa)	ρ_y(%)	f_{yy} (MPa)	V_{exp} (kN)	V_{pred}(kN)	$\frac{V_{exp}}{V_{pred}}$
42	V6CC	0.152	0.305	1.52	6.09	20.5	25	3.52	400	0	–	44.48	48.49	0.92
43	V3EC	0.152	0.305	1.83	7.16	18.8	25	1.67	379	0	–	37.81	32.1	1.18
44	V4EC	0.152	0.305	1.83	7.2	21.2	25	2.18	394	0	–	41.81	41.01	1.02
45	V5EC	0.152	0.305	1.83	7.24	19.5	25	2.78	370	0	–	39.59	38.05	1.04
46	V6EC	0.152	0.305	1.83	7.3	19.1	25	3.52	400	0	–	42.26	36.74	1.15
47	V3GC	0.152	0.305	2.13	8.35	22.4	25	1.67	379	0	–	31.58	35.06	0.9
48	V4GC	0.152	0.305	2.13	8.4	21	25	2.18	394	0	–	36.92	33.85	1.09
49	V5GC	0.152	0.305	2.13	8.45	21.9	25	2.78	370	0	–	41.81	36.8	1.14
50	V6GC	0.152	0.305	2.13	8.52	21.4	25	3.52	400	0	–	40.48	36.25	1.12
51	V3JC	0.152	0.305	2.44	9.54	22.2	25	1.67	379	0	–	28.02	25.75	1.09
52	V4JC	0.152	0.305	2.44	9.6	22.2	25	2.18	394	0	–	31.58	31.02	1.02
53	V5JC	0.152	0.305	2.44	9.66	22.8	25	2.78	370	0	–	40.03	33.48	1.2
54	V6JC	0.152	0.305	2.44	9.74	21.4	25	3.52	400	0	–	35.14	32.65	1.08
55	VII6C	0.152	0.305	0.91	3.62	20.1	25	2.78	370	0	–	51.15	62.75	0.82
56	VIII3AAC	0.152	0.305	0.91	3.58	34.5	25	1.67	379	0	–	55.6	60.42	0.92
57	VIII4AAC	0.152	0.305	0.91	3.6	29.2	25	2.18	394	0	–	57.83	60.25	0.96
58	VIII5AAC	0.152	0.305	0.91	3.62	32.8	25	2.78	370	0	–	56.94	74.66	0.76
59	VIII6AAC	0.152	0.305	0.91	3.65	34.4	25	3.52	400	0	–	60.05	82.72	0.73
60	VIII3AC	0.152	0.305	1.22	4.77	31.8	25	1.67	379	0	–	53.38	55.27	0.97
61	VIII4AC	0.152	0.305	1.22	4.8	30.5	25	2.18	394	0	–	53.82	63.87	0.84
62	VIII5AC	0.152	0.305	1.22	4.83	32.8	25	2.78	370	0	–	54.27	73.22	0.74
63	VIII6AC	0.152	0.305	1.22	4.87	34.1	25	3.52	400	0	–	59.16	69.77	0.85
64	VIII4CC	0.152	0.305	1.52	6	38.4	25	2.18	394	0	–	52.49	60.85	0.86
65	VIII5CC	0.152	0.305	1.52	6.04	37.4	25	2.78	370	0	–	57.38	67.6	0.85
66	VIII6CC	0.152	0.305	1.52	6.09	38.4	25	3.52	400	0	–	63.16	79.17	0.8
67	VIII4EC	0.152	0.305	1.83	7.2	36.8	25	2.18	394	0	–	51.6	48.28	1.07
68	VIII5EC	0.152	0.305	1.83	7.24	37.4	25	2.78	370	0	–	53.38	55.48	0.96
69	VIII6EC	0.152	0.305	1.83	7.3	33.8	25	3.52	400	0	–	48.93	63.15	0.77
70	IX3AAC	0.152	0.305	0.91	3.58	12.5	25	1.67	379	0	–	40.48	42.07	0.96
71	IX4AAC	0.152	0.305	0.91	3.6	12.9	25	2.18	394	0	–	42.7	37.91	1.13
72	IX5AAC	0.152	0.305	0.91	3.62	15.4	25	2.78	370	0	–	50.26	56.8	0.88
73	IX6AAC	0.152	0.305	0.91	3.65	13.4	25	3.52	400	0	–	62.28	51.92	1.2
74	IX3AC	0.152	0.305	1.22	4.77	13.7	25	1.67	379	0	–	36.92	41.92	0.88
75	IX4AC	0.152	0.305	1.22	4.8	12.9	25	2.18	394	0	–	40.03	40.3	0.99
76	IX5AC	0.152	0.305	1.22	4.83	15.4	25	2.78	370	0	–	43.59	48.86	0.89
77	IX6AC	0.152	0.305	1.22	4.87	12.4	25	3.52	400	0	–	40.92	38.73	1.06
78	IX3CC	0.152	0.305	1.52	5.96	12.2	25	1.67	379	0	–	31.14	31.42	0.99
79	IX4CC	0.152	0.305	1.52	6	17.1	25	2.18	394	0	–	35.14	41.6	0.84
80	IX5CC	0.152	0.305	1.52	6.04	14.7	25	2.78	370	0	–	34.25	37.98	0.9
81	IX6CC	0.152	0.305	1.52	6.09	13.7	25	3.52	400	0	–	39.59	35.83	1.1
82	IX4EC	0.152	0.305	1.83	7.2	14.3	25	2.18	394	0	–	35.59	30.29	1.17
83	IX5EC	0.152	0.305	1.83	7.24	15.1	25	2.78	370	0	–	34.7	31.84	1.09
84	XC	0.203	0.533	1.52	3.16	16.8	25	1.4	394	0	–	84.52	88.29	0.96
85	XIPCa	0.152	0.305	1.83	7.3	36.3	25	3.52	400	0	–	53.38	66.18	0.81
86	XIPCb	0.152	0.305	1.83	7.3	36.3	25	3.52	400	0	–	53.38	66.18	0.81
87	SIOCa	0.152	0.305	1.52	6	35.7	25	2.18	394	0	–	48.49	56.94	0.85
88	SIOCb	0.152	0.305	1.52	6	39	25	2.18	394	0	–	52.49	58.29	0.9
89	SIIOCa	0.254	0.508	1.83	4.01	38.3	25	2	370	0	–	146.8	157.8	0.93
90	SIIOCb	0.254	0.508	1.83	4.01	38.3	25	2	370	0	–	133.4	157.8	0.85
91	SI-23–5	0.152	0.305	1.52	6	38.5	25	2.18	394	0.475	341	60.94	57.47	1.06
92	SI-26a	0.152	0.305	1.52	6	34.7	25	2.18	394	0.277	341	59.61	56.9	1.05
93	SI-26b	0.152	0.305	1.52	6	34.7	25	2.18	394	0.277	341	62.28	56.9	1.09
94	SI-210a	0.152	0.305	1.52	6	38	25	2.18	394	0.166	341	60.5	55.2	1.1
95	SI-210b	0.152	0.305	1.52	6	38	25	2.18	394	0.166	341	63.16	58.38	1.08
96	SI-210c	0.152	0.305	1.52	6	39	25	2.18	394	0.166	341	66.72	58.96	1.13
97	SI-212a	0.152	0.305	1.52	6	39.5	25	2.18	394	0.139	341	64.94	59.17	1.1
98	SI-212b	0.152	0.305	1.52	6	39.5	25	2.18	394	0.139	341	68.95	59.17	1.17
99	SII-24–1	0.254	0.508	1.83	4.01	37.3	25	2	370	0.249	341	244.7	223.1	1.1
100	SII-26–1	0.254	0.508	1.83	4.01	40.1	25	2	370	0.166	341	206.8	208.9	0.99
101	SII-29a-1	0.254	0.508	1.83	4.01	38.8	25	2	370	0.111	341	159.7	158.8	1.01
102	SII-29b-1	0.254	0.508	1.83	4.01	37.6	25	2	370	0.111	341	160.1	181.5	0.88
103	SII-213–5-1	0.254	0.508	1.83	4.01	38.9	25	2	370	0.074	341	148.1	169.2	0.88
104	SII-24–5-2	0.254	0.508	1.83	4.01	37.6	25	2	370	0.222	372	243.8	222.4	1.1
105	SII-29a-2	0.254	0.508	1.83	4.01	37.2	25	2	370	0.111	372	216.6	183.9	1.18
106	SII-29b-2	0.254	0.508	1.83	4.01	41.4	25	2	370	0.111	372	202.4	190.9	1.06
107	SII-29c-2	0.254	0.508	1.83	4.01	24.1	25	2	370	0.111	372	161.5	162	1
108	SII-29d-2	0.254	0.508	1.83	4.01	30.4	25	2	370	0.111	372	165	174.2	0.95
109	SII-29e-2	0.254	0.508	1.83	4.01	48.5	25	2	370	0.111	372	206.4	201.1	1.03
110	SII-29f-2	0.254	0.508	1.83	4.01	41.8	25	2	370	0.111	372	234.4	191	1.23
111	SII-29 g-2	0.254	0.508	1.83	4.01	15.7	25	2	370	0.111	372	149.9	142.4	1.05
112	SII-213-5a-2	0.254	0.508	1.83	4.01	37	25	2	370	0.074	372	161.5	167.6	0.96
113	SII-218a-2	0.254	0.508	1.83	4.01	37.6	25	2	370	0.055	372	164.1	165.9	0.99
114	SII-24–5-3	0.254	0.508	1.83	4.01	35.4	25	2	370	0.222	237	232.6	198.9	1.17
115	SII-29–3	0.254	0.508	1.83	4.01	34.3	25	2	370	0.111	237	177.9	162.9	1.09
116	SII-39–1	0.254	0.508	1.83	4.01	37.2	25	2	370	0.245	517	248.2	222.7	1.11

(*continued on next page*)

(*continued*)

F6No.	ID	b (m)	h (m)	L_s(m)	$\frac{a}{d}$	f'_c(MPa)	a_g(mm)	ρ_x(%)	f_{yx}(MPa)	ρ_y(%)	f_{yy} (MPa)	V_{exp} (kN)	V_{pred}(kN)	$\frac{V_{exp}}{V_{pred}}$
117	SII-313–5-1	0.254	0.508	1.83	4.01	37.2	25	2	370	0.164	517	251.3	219	1.15
118	SII-318–1	0.254	0.508	1.83	4.01	40.5	25	2	370	0.123	517	220.2	218	1.01
119	SII-321–1	0.254	0.508	1.83	4.01	38.7	25	2	370	0.105	517	163.7	202.4	0.81
120	SII-39–2	0.254	0.508	1.83	4.01	37.1	25	2	370	0.245	352	248.7	220.8	1.13
121	SII-313–5-2	0.254	0.508	1.83	4.01	39.6	25	2	370	0.164	352	234.9	209.5	1.12
122	SII-318–2	0.254	0.508	1.83	4.01	38.9	25	2	370	0.123	352	177	190.5	0.93
123	SII-321–2	0.254	0.508	1.83	4.01	38	25	2	370	0.105	352	166.8	143.7	1.16
124	SII-39–3	0.254	0.508	1.83	4.01	42.7	25	2	370	0.245	276	239.8	227.1	1.06
125	SII-313–5-3	0.254	0.508	1.83	4.01	42.7	25	2	370	0.164	276	213.5	199	1.07
126	SII-318–3	0.254	0.508	1.83	4.01	43	25	2	370	0.123	276	174.8	184.4	0.95
127	SII-321–3	0.254	0.508	1.83	4.01	43	25	2	370	0.105	276	140.6	179.5	0.78
Lefas et al. (1990) – Shear walls														
128	SW21	0.065	0.65	1.3	2	35.7	10	3.3	470	0.8	520	127	119	1.07
129	SW22 (N = 182 kN)	0.065	0.65	1.3	2	42.2	10	3.3	470	0.8	520	150	143	1.05
130	SW23 (N = 343 kN)	0.065	0.65	1.3	2	39.8	10	3.3	470	0.8	520	180	163.5	1.1
131	SW24	0.065	0.65	1.3	2	40.3	10	3.3	470	0.8	520	120	122	0.98
132	SW25 (N = 325 kN)	0.065	0.65	1.3	2	37.5	10	3.3	470	0.8	520	150	155	0.97
133	SW26	0.065	0.65	1.3	2	25.1	10	3.3	470	0.4	520	123	123	1
Angekolas et al. (2001) – Simply supported beams														
134	DB0.530	0.3	1	2.7	2.92	32	10	0.5	550	0	–	165	134	1.23
135	DB120	0.3	1	2.7	2.92	21	10	1.01	550	0	–	179	170.5	1.05
136	DB130	0.3	1	2.7	2.92	32	10	1.01	550	0	–	185	176.3	1.05
137	DB140	0.3	1	2.7	2.92	38	10	1.01	550	0	–	180	181.2	0.99
138	DB230	0.3	1	2.7	2.92	32	10	2.09	550	0	–	257	243.2	1.06
139	DB120M	0.3	1	2.7	2.92	21	10	1.01	[435 550]	0.402	508	282	315.4	0.89
140	DB140M	0.3	1	2.7	2.92	38	10	1.01	[435 550]	0.402	508	277	392.6	0.71
141	DB0.530 M	0.3	1	2.7	2.92	32	10	0.5	[435 550]	0.402	508	263	255.4	1.03
Vecchio and Shim (2004) – Simply supported beams														
142	VS-OA1	0.305	0.552	1.83	4	22.6	20	1.43	[445 436]	0	–	165.5	150.9	1.1
143	VS-OA2	0.305	0.552	2.29	5	25.9	20	1.84	[440 436]	0	–	160	169.7	0.94
144	VS-OA3	0.305	0.552	3.2	7	43.5	20	2.26	[445 436]	0	–	192.5	189.8	1.01
145	VS-A1	0.305	0.552	1.83	4	22.6	20	1.6	[315 445 436]	0.1	600	229.5	228.1	1.01
146	VS-A2	0.305	0.552	2.29	5	25.9	20	2.02	[315 440 436]	0.1	600	219.5	230.4	0.95
147	VS-A3	0.305	0.552	3.2	7	43.5	20	2.49	[315 445 436]	0.1	600	210	210.2	1
148	VS-B1	0.229	0.552	1.83	4	22.6	20	2.22	[315 445 436]	0.148	600	217	219.3	0.99
149	VS-B2	0.229	0.552	2.29	5	25.9	20	2.22	[315 440 436]	0.148	600	182.5	179.8	1.01
150	VS-B3	0.229	0.552	3.2	7	43.5	20	2.77	[315 445 436]	0.147	600	171	166.8	1.03
151	VS-C1	0.152	0.552	1.83	4	22.6	20	2.15	[315 436]	0.202	600	141	130.9	1.08
152	VS-C2	0.152	0.552	2.29	5	25.9	20	3.34	[315 440 436]	0.202	600	145	158.5	0.91
153	VS-C3	0.152	0.552	3.2	7	43.5	20	3.34	[315 445 436]	0.201	600	132.5	138.7	0.95
Sherwood et al. (2007) – Simply supported beams														
154	SB10N1	0.3	1.51	4.05	2.89	38.4	10	0.83	[487 452]	0	–	277	233.6	1.19
155	SB10N2	0.3	1.51	4.05	2.89	40.3	10	0.83	[487 452]	0	–	254	233.6	1.09
156	SB20N1	0.3	1.51	4.05	2.89	31.4	20	0.83	[487 452]	0	–	277	238.6	1.16
157	SB20N2	0.3	1.51	4.05	2.89	33.2	20	0.83	[487 452]	0	–	277	238.7	1.16
158	SB40N1	0.3	1.51	4.05	2.89	28.1	40	0.83	[487 452]	0	–	254	237.9	1.07
159	SB40N2	0.3	1.51	4.05	2.89	28.5	40	0.83	[487 452]	0	–	300	237.9	1.26
160	SB50N1	0.3	1.51	4.05	2.89	41	50	0.83	[487 452]	0	–	283	238.6	1.19
161	SB50N2	0.3	1.51	4.05	2.89	40.1	50	0.83	[487 452]	0	–	310	238.6	1.3
162	SSB10N1	0.122	0.33	0.81	2.89	41.9	10	0.83	494	0	–	36.6	39.77	0.92
163	SSB10N2	0.122	0.33	0.81	2.89	41.9	10	0.83	494	0	–	38.3	39.77	0.96
164	SSB20N1	0.122	0.33	0.81	2.89	39.2	20	0.83	494	0	–	39.1	39.77	0.98
165	SSB20N2	0.122	0.33	0.81	2.89	38.1	20	0.83	494	0	–	38.2	39.77	0.96
166	SSB40N1	0.122	0.33	0.81	2.89	29.1	40	0.83	494	0	–	41.9	39.77	1.05
167	SSB40N2	0.122	0.33	0.81	2.89	29.1	40	0.83	494	0	–	34.9	39.6	0.88
													Mean	0.99
													COV (%)	12.8

References

[1] Navarro-Gregori J, Miguel PF, Fernández MA, Martí-Vargas JR. A theoretical model for including the effect of monotonic shear loading in the analysis of reinforced concrete beams. Eng Struct 2013;52:257–72.

[2] Ceresa P, Petrini L, Pinho R. Flexure-shear fibre beam-column elements for modeling frame structures under seismic loading - state of the Art. J Earthquake Eng 2007;11:46–88.

[3] Li Z-X, Gao Y, Zhao Q. A 3D flexure–shear fiber element for modeling the seismic behavior of reinforced concrete columns. Eng Struct 2016;117:372–83.

[4] Feng D-C, Wu G, Sun Z-Y, Xu J-G. A flexure-shear Timoshenko fiber beam element based on softened damage-plasticity model. Eng Struct 2017;140:483–97.

[5] Saritas A. Modeling of inelastic behaviour of curved members with a mixed formulation beam element. Finite Elem Anal Des 2009;45(5):357–68.

[6] Taylor RL, Filippou FC, Saritas A, Auricchio F. A mixed finite element method for beam and frame problems. Comput Mech 2003;31(1-2):192–203.

[7] Saritas A, Filippou FC. Inelastic axial-flexure-shear coupling in a mixed formulation beam finite element. Int J Non Linear Mech 2009;44(8):913–22.

[8] Menegotto M, Pinto PE. Method of analysis for cyclically loaded reinforced concrete plane frames including changes in geometry and non-elastic behaviour of elements under combined normal force and bending. In: IABSE symposium on resistance and ultimate deformability of structures acted on by well-defined repeated loads. Lisbon, Portugal; 1973.

[9] Kaba S, Mahin SA. Refined modeling of reinforced concrete columns for seismic analysis. EERC Report 84/03, Earthquake Engineering Research Center, University of California, Berkeley; 1984.
[10] Zeris CA, Mahin SA. Analysis of reinforced concrete beam-columns under uniaxial excitation. J Struct Eng 1988;114(4):804–20.
[11] Zeris CA, Mahin SA. Behaviour of reinforced concrete structures subjected to biaxial excitation. J Struct Eng 1991;117(9):2657–73.
[12] Zeris CA. Three dimensional nonlinear response of reinforced concrete buildings. PhD thesis, University of California, Department of Civil Engineering, Berkeley; 1986.
[13] Ciampi V, Carlesimo LA nonlinear beam element for seismic analysis of structures. In: Proceedings of the 8th European Conference on Earthquake Engineering. Lisbon, Portugal; 1986.
[14] Remino M. Shear modelling of reinforced concrete structures. Ph.D. Thesis, Dipartimento di Ingegneria Civile, Universita degli Studi di Brescia, Brescia, Italy; 2004.
[15] Mohr S, Bairán JM, Marí AR. A frame element model for the analysis of reinforced concrete structures under shear and bending. Eng Struct 2010;32(12):3936–54.
[16] Du Z-L, Ding Z-X, Liu Y-P, Chan S-L. Advanced flexibility-based beam-column element allowing for shear deformation and initial imperfection for direct analysis. Eng Struct 2019;199:109586. https://doi.org/10.1016/j.engstruct.2019.109586.
[17] Sae-Long W, Limkatanyu S, Hansapinyo C, Imjai T, Kwon M. Forced-based Shear-flexure-interaction Frame Element for Nonlinear Analysis of Non-ductile Reinforced Concrete Columns. Journal of Applied and Computational Mechanics 2020; 6(Special Issue):1151-1167.
[18] Kalliontzis D, Shing PB. Force-based frame element with axial force-flexure-shear interaction for modelling reinforced concrete members. ACI Struct J 2021;118(3): 131–46.
[19] Spacone E, Ciampi V, Filippou FC. A beam element for seismic damage analysis. EERC Report 92/08, Earthquake Engineering Research Center, University of California, Berkeley; 1992.
[20] Spacone E, Filippou FC, Taucer FF. Fibre beam-column model for non-linear analysis of R/C frames: Part I. Formulation. Earthq Eng Struct Dyn 1996;25(7): 711–25.
[21] Spacone E, Filippou FC, Taucer FF. Fibre beam-column model for non-linear analysis of R/C frames: Part II. Applications. Earthq Eng Struct Dyn 1996;25(7): 727–42.
[22] McKenna F, Fenves GL, Scott M. H. Open System for Earthquake Engineering Simulation. University of California, Berkeley; 2000.
[23] Guner S, Vecchio FJ. Pushover analysis of shear-critical frames: formulation. ACI Struct J 2010;107(1):63–71.
[24] Guner S, Vecchio FJ. Pushover analysis of shear-critical frames: application. ACI Struct J 2010;107(1):72–81.
[25] Vecchio FJ. Disturbed stress field model for reinforced concrete: formulation. J Struct Eng 2000;126(9):1070–7.
[26] Guner S. Performance Assessment of Shear-Critical Reinforced Concrete Plane Frames. PhD thesis, Department of Civil Engineering, University of Toronto, Toronto, ON, Canada; 2008.
[27] Rajapakse RMCM, Wijesundara KK, Nascimbene R, Bandara CS, Dissanayake PBR. Accounting axial-moment-shear interaction for force-based fibre modeling of RC frames. Eng Struct 2019;184:15–36.
[28] Vecchio FJ, Collins MP. The modified compression field theory for reinforced concrete elements subjected to shear. ACI Journal 1986;83(2):219–31.
[29] Vecchio FJ, Collins MP. Predicting the response of reinforced concrete beams subjected to shear using modified compression field theory. ACI Struct J 1988;85 (3):258–68.
[30] Petrangeli M. Fibre element for cyclic bending and shear of RC structures. II: verification. J Eng Mech 1999;125(9):1002–9.
[31] Hippola S, Rajapakse C, Mihaylov B, Wijesundara K. A force-based fiber beam-column element to predict moment-axial-shear interaction of reinforced concrete frames. Struct Concr 2021;22:2466–81.
[33] Hippola HMSS, Rajapakse RMCM, Wijesundara KK, Dissanayake PBR. Modification of force-based fibre beam-column element formulation to cater highly localized nonlinear behaviour. Proceedings of the 7th ECCOMAS Thematic Conference on Computational Methods in Structural Dynamics and Earthquake Engineering, Crete, Greece; 2019.
[34] Bentz EC. Sectional Analysis of Reinforced Concrete Members. Ph.D. Dissertation, Department of Civil Engineering, University of Toronto, Toronto, ON, Canada; 2000.
[35] Kent DC, Park R. Flexural Members with Confined Concrete. ASCE J Struct Div 1971;97:1341–60.
[36] Okamura H, Maekawa K. Nonlinear analysis and constitutive models of reinforced concrete. Tokyo: Giho-do Press; 1991.
[37] Vecchio FJ. Disturbed stress field model for reinforced concrete: implementation. J Struct Eng 2001;127(1):12–20.
[38] Bresler B, Scordelis AC. Shear strength of reinforced concrete beams. J ACI 1963;60 (1):51–72.
[39] Krefeld WJ, Thurston CW. Studies of the shear and diagonal tension strength of simply supported reinforced concrete beams. ACI J 1966;63(4):451–76.
[40] Lefas ID, Kotsovos MD, Ambraseys NN. Behaviour of reinforced concrete structural walls: strength, deformation characteristics, and failure mechanism. ACI Struct J 1990;93:23–31.
[41] Vecchio FJ, Balopoulou S. On the nonlinear behaviour of reinforced concrete frames. Can J Civ Eng 1990;17(5):698–704.
[42] Vecchio FJ, Emara MB. Shear deformations in reinforced concrete frames. ACI Struct J 1992;89:46–56.
[43] Angelakos D, Bentz EC, Collins MP. Effect of concrete strength and minimum stirrups on shear strength of large members. ACI Struct J 2001;98(3):290–300.
[44] Vecchio FJ, Shim W. Experimental and analytical reexamination of classic concrete beam tests. ASCE J Struct Eng 2004;130(3):460–9.
[45] Duong KV, Sheikh SA, Vecchio FJ. Seismic behaviour of shear-critical reinforced concrete frame: experimental investigation. ACI Struct J 2007;104(3):304–13.
[46] Sherwood E, Bentz E, Collins MP. Effect of aggregate size on beam-shear strength of thick slabs. ACI Struct J 2007;104:180–90.